

1 Analysis of secondary inorganic aerosols over the Greater Area of 2 Athens using the EPISODE-CityChem source dispersion and 3 photochemistry model

4 Stelios Myriokefalitakis¹, Matthias Karl², Kim A. Weiss^{1,3}, Dimitris Karagiannis¹, Eleni
5 Athanopoulou¹, Anastasia Kakouri¹, Aikaterini Bougiatioti¹, Eleni Liakakou¹, Iasonas Stavroulas¹,
6 Georgios Papangelis¹, Georgios Grivas¹, Despina Paraskevopoulou¹, Orestis Speyer¹, Nikolaos
7 Mihalopoulos¹, and Evangelos Gerasopoulos¹

8 ¹ Institute for Environmental Research and Sustainable Development (IERSD), National Observatory of Athens, Penteli,
9 Greece

10 ² Helmholtz-Zentrum Hereon GmbH, Geesthacht, Germany

11 ³ Natural Sciences, Institute of Physics and Meteorology, Earth and Climate System Sciences, Universität Hohenheim,
12 Stuttgart, Germany

13
14 Correspondence to: Stelios Myriokefalitakis (steliosm@noa.gr) and Matthias Karl (matthias.karl@hereon.de)

15 **Abstract.** Secondary inorganic aerosols (SIA) are major components of fine particulate matter (PM_{2.5}), having substantial
16 implications for climate and air quality in an urban environment. In this study, a state-of-the-art thermodynamic model has
17 been coupled to the source dispersion and photochemistry city-scale chemistry transport model EPISODE-CityChem, able to
18 simulate pollutants on a horizontal resolution of 100 x 100 m², to determine the equilibrium between the inorganic gas and
19 aerosol phases over the Greater Area of Athens, Greece, for the year 2019. In agreement with in-situ observations, sulfate
20 (SO₄²⁻) is calculated to have the highest annual mean surface concentration (2.15 ± 0.88 μg m⁻³) among SIA in the model
21 domain, followed by ammonium (NH₄⁺; 0.58 ± 0.14 μg m⁻³) and fine nitrate (NO₃⁻; 0.24 ± 0.22 μg m⁻³). Simulations denote
22 that NO₃⁻ formation strongly depends on the local nitrogen oxide emissions, along with the ambient temperature, the relative
23 humidity, and the photochemical activity. Additionally, we show that anthropogenic combustion sources may have an
24 important impact on the NO₃⁻ formation in an urban area. During the cold period, the combined effect of decreased temperature
25 in the presence of non-sea salt potassium favors the partitioning of HNO₃ in the aerosol phase in the model, raising the NO₃⁻
26 formation in the area. Overall, this work highlights the significance of atmospheric composition and the local meteorological
27 conditions for the equilibrium distribution of nitrogen-containing semivolatile compounds and the acidity of inorganic
28 aerosols, especially in urban areas where atmospheric trace elements from natural and anthropogenic sources coexist.

29 **1 Introduction**

30 Fine particulate matter (PM_{2.5}) impacts the planet's radiative balance (Myhre et al., 2014) and severely affects air quality
31 (WHO, 2021). Such effects strongly depend on the chemical and physical properties of PM_{2.5}, e.g., shape, size distribution,
32 and hygroscopicity. Among other particulate pollutants, like organic matter, elemental carbon, dust particles, and sea spray,
33 secondary inorganic aerosols (SIAs) are identified as a critical PM_{2.5} fraction in an urban atmosphere. SIAs are formed in the
34 atmosphere via gas-to-particle conversion of precursors of anthropogenic (e.g., coal combustion, biomass burning, vehicular),
35 biomass burning, and natural (e.g., marine, soil, lightning, volcanoes) origin, with sulfate (SO₄²⁻), nitrate (NO₃⁻), and
36 ammonium (NH₄⁺) being the three major SIA species. However, primary emissions, such as those from residential combustion,
37 have been found to increase their atmospheric abundance (Zhang et al., 2023). SIAs may further contribute significantly to air
38 quality degradation; for example, sulfates can reduce visibility and contribute to acid rain (Liu et al., 2019), affecting forest
39 and aquatic ecosystems (Driscoll et al., 2003, 2016), and damaging building materials (Ozga et al., 2013). On the other hand,
40 SIAs are also linked to increased asthma exacerbation (Sarnat et al., 2015) and cardiovascular hospitalization (Basagaña et al.,
41 2015) and can contribute to human mortality via the enhancement of fine particulate air pollution (Franklin et al., 2008; Pope
42 et al., 2020). Focusing, in particular, on polluted environments, Nenes et al. (2020) indicated that atmospheric acidity, aerosol
43 liquid water content (LWC), and meteorological conditions (temperature and relative humidity) are the main parameters that
44 control SIA formation sensitivity, depending on ammonia (NH₃) and nitric acid (HNO₃) availability.

45 Sulfates are primarily formed by the oxidation of sulfur dioxide (SO₂) as a byproduct of fossil fuel burning, such as coal and
46 oil in power plants and industrial processes, as well as residual oil burning in shipping. In the gas phase, the SO₂ homogeneous
47 oxidation via OH radicals during daytime strongly depends on temperature, while the heterogeneous oxidation of SO₂ via
48 H₂O₂/O₃ may proceed in aqueous media such as cloud liquid water and in-cloud scavenging processes (Seinfeld and Pandis,
49 2006), enhanced in the presence of transition metal ions (e.g., Mn²⁺ and Fe³⁺; Alexander et al., 2009), and/or on aerosol surfaces
50 such as dust aerosols (Wang et al., 2022). Aqueous phase processes are nevertheless found to be responsible for about two-
51 thirds of the total sulfate production in the global troposphere (e.g., Myriokefalitakis et al., 2022). Overall, it is well established
52 that the amounts of precursor gases and oxidants, the cloud cover, the amount of available surface area, and meteorological
53 factors such as temperature and relative humidity all affect the rate of SO₂ conversion to sulfate (Liu et al., 2021).

54 Particulate nitrate formation depends on the emissions of nitrogen oxides (NO_x) from traffic, power plants, and industrial
55 activities, along with the gas-phase concentrations of ammonia (NH₃) as emitted by agricultural activities, waste management,
56 industrial processes, and the biosphere. The formation of NO₃⁻ is, however, a rather complex process, strongly dependent on
57 interactions of acidity, relative humidity, and temperature (Guo et al., 2017b; Nenes et al., 2020), with the partitioning of HNO₃
58 to the particulate phase enhanced under lower ambient temperatures (Guo et al., 2017b). Nevertheless, since ammonium nitrate
59 (NH₄NO₃) is formed when NH₃ is in excess upon the formation of ammonium sulfate and ammonium bisulfate, such an
60 equilibrium, besides the availability of NH₃, also depends on the concentration of sulfuric acid (H₂SO₄). The relative humidity
61 is, nevertheless, a key factor for SIA formation, determining the aerosol LWC and thus the aerosol acidity levels, which in

62 turn impact the HNO_3 partitioning in the aerosol phase. All in all, NO_3^- formation increases the aerosol LWC by lowering
63 aerosol acidity via dilution and thus further promoting HNO_3 partitioning into the particulate phase (Guo et al., 2017a).

64 Thermodynamic calculations (Clegg et al., 1998; Fountoukis and Nenes, 2007; Nenes et al., 1998) are considered to be the
65 appropriate way of assessing non-linearities in an inorganic aerosol system and the behavior of a non-ideal liquid solution.
66 Such methods can explicitly account for the equilibrium state of inorganic particles by calculating the gas- and particulate-
67 phase fractions of the inorganics, along with the corresponding aerosol LWC and the respective levels of acidity (pH), both of
68 which are very important for assessing the burden of the secondary inorganic PM fraction. The presence of nonvolatile cations
69 (NVCs) in thermodynamic calculations, however, has been shown to substantially affect the ion balance (Guo et al., 2018) and
70 thus the partitioning of $\text{HNO}_3/\text{NO}_3^-$ and $\text{NH}_3/\text{NH}_4^+$ species, especially in areas with abundant mineral dust and sea spray
71 aerosols (Athanasopoulou et al., 2008, 2016), such as the Eastern Mediterranean. For example, calcium-containing dust
72 particles may react with nitric acid to form calcium nitrate ($\text{Ca}(\text{NO}_3)_2$), significantly enhancing NO_3^- formation, especially
73 when natural and anthropogenic particulate matter coexist. On the other hand, NVCs from combustion sources related to
74 natural or anthropogenic activities may also critically impact the predictions of inorganic partitioning between the gas and the
75 particulate phase in an urban environment (Cheng et al., 2022).

76 Regional chemistry transport models (CTM) are promising tools for providing spatial information on environmental impacts
77 occurring in the urban landscape. Although such modeling tools can successfully simulate the inorganic and organic
78 components of atmospheric aerosols at the background scale (e.g., Brandt et al., 2003; Athanasopoulou et al., 2013; Zakoura
79 and Pandis, 2018; Basla et al., 2022), they are not rather accurate in the representation of their spatial distribution in proximity
80 to point and/or line sources (Santiago et al., 2022). On the contrary, urban-scale CTM models have the advantage of mapping
81 air pollution levels in high-resolution ($\leq 1\text{km}$) (e.g., Hurley et al., 2005; Karl et al., 2019; Denby et al., 2020), although critical
82 processes related to air quality, such as aerosol representation and its chemical speciation, may still be simplistically
83 represented due to the high computational load of such modeling systems. Indeed, urban-scale CTMs usually estimate the bulk
84 mass of particulate matter ($\text{PM}_{2.5}$ and/or PM_{10}) without having incorporated their chemical interactions with gaseous pollutants
85 in the atmosphere, like in the case of inorganic chemical components in the aqueous and/or solid state. Such a simplistic aerosol
86 parameterization in local/city-scale models, which still remains a common approach, nevertheless represents the next
87 challenging issue of multi-scale modeling (Sokhi et al., 2022).

88 Several regional-scale numerical simulations of atmospheric pollution have been performed over the Eastern Mediterranean
89 area (Athanasopoulou et al., 2015; Fountoukis et al., 2011; Im et al., 2013; Kontos et al., 2021; Kushta et al., 2019; Liora et
90 al., 2022), focusing in particular on the urban area of Athens, one of the most polluted cities in the EU. Most of these studies
91 highlight the complex interactions among nitrogen and sulfur oxides of anthropogenic origin with sea salt and/or dust particles
92 of natural origin over the area (Athanasopoulou et al., 2008; Karydis et al., 2016). These findings are also confirmed by several
93 local observational studies (Bardouki et al., 2003; Dimitriou et al., 2021; Koçak et al., 2004, 2012; Stavroulas et al., 2021). On
94 the other hand, recent city-scale modeling studies over Athens (Gratsea et al., 2021; Grivas et al., 2020; Lasne et al., 2023;

95 Ramacher et al., 2021) clearly demonstrate the difficulties in simulating the inorganic constituents of atmospheric aerosols in
96 the area, in particular at the intra-urban scale.

97 To tackle the above challenges in the context of multi-pollutant studies at a city-scale spatial resolution, we here develop a
98 framework for fine aerosol thermodynamic calculations to better understand the SIA formation mechanisms in an urban
99 environment. Section 2 provides an overview of the model, focusing mostly on the new developments applied in this study. In
00 particular, we describe the aqueous-phase chemistry scheme used to simulate the atmospheric SO_4^{2-} production in cloud
01 droplets, the respective developments for the thermodynamic calculations of semi-volatile inorganics, along with a series of
02 code updates currently applied in the model. In Sect. 3, we present the model-derived SO_4^{2-} , NO_3^- , and NH_4^+ surface
03 concentrations and their evaluation against in situ observations. Finally, in Sect. 4, we discuss the simulated processes and
04 summarize the implications of explicitly resolving the secondary formation of $\text{PM}_{2.5}$ in a city-scale chemistry transport model
05 for air quality, as well as the plans for future model development.

06 **2. Methodology and Data**

07 The numerical atmospheric model system used for this study is the chemistry-transport model (CTM) EPISODE-CityChem
08 (Karl et al., 2019), coupled here to atmospheric processes relevant to SIA formation. The model is applied over the Greater
09 Area of Athens (Greece), centered at the urban center (Fig. 1), horizontally covering a domain of $45 \times 45 \text{ km}^2$ (SW corner
10 23.4E° , 37.8N° , $1 \times 1 \text{ km}^2$ cell size, with a subgrid of 100 m) and vertically representing a 24-layered atmosphere up to 3.7
11 km. For the current study, simulations of air quality are performed for 2019. Three simulations have been conducted in this
12 work to investigate uncertainties regarding the impact of SIA formation in the Greater Area of Athens (GAA): i) the base
13 simulation where a complete chemistry/thermodynamic scheme is accounted in the model (W/ SIA); ii) a simulation where
14 the secondary production of SO_4^{2-} , NO_3^- , and NH_4^+ is neglected (W/O SIA), that is focused on the impact of long-range
15 transport to SIA concentrations in the study area; and iii) an extra simulation where the impact of NVC emissions related to
16 domestic burning on the SIA formation is neglected (W/O Kbb), focusing thus on the importance of potassium (K^+) on the
17 equilibrium distribution of nitrogen-containing semivolatile compounds. Finally, available in situ measurements for the area
18 and year of study are used to assess the accuracy of model predictions and the efficiency of the performed advancements.

19 **2.1 The EPISODE-CityChem model**

20 EPISODE-CityChem is a city-scale CTM designed for treating complex atmospheric chemistry in urban areas and improving
21 the representation of near-field dispersion. EPISODE is an Eulerian dispersion model developed by the Norwegian Institute
22 for Air Research (Slørdal et al., 2007) to simulate pollutant dispersion at the city scale and microscale simultaneously.
23 EPISODE consists of a 3-D Eulerian grid that interacts with a subgrid Gaussian dispersion model for the dispersion of
24 pollutants emitted from both line and point sources (Hamer et al., 2020), allowing the retrieval of pollutant concentrations at
25 the subgrid scale in an urban area. The CityChem extension offers an explicit description of the gaseous reactive pollutants'

26 photochemistry on the Eulerian grid, along with the dispersion close to point emission sources (e.g., industrial stacks) and line
27 emission sources (open roads and streets). For this work, however, supplementary emissions are incorporated into the model
28 domain (see Sect. 2.1.3) to enable a realistic simulation of SIA formation.

29 **2.1.1 Gas-phase chemistry**

30 EPISODE-CityChem has several schemes for solving the chemistry of the gas phase. For the standard model configuration,
31 the updated chemistry scheme, EmChem09-HET, is applied on the coarse grid, which supports more than 100 reactions,
32 including photodissociation, thermal, and heterogeneous reactions, and about 70 species. However, for this study, the well-
33 documented Carbon Bond Mechanism 2005 (CB05; Yarwood et al., 2005), along with more recent modifications (mCB05) as
34 introduced by Williams et al. (2013, 2017) are applied. For comparison, we note that the mCB05 configuration here uses 50
35 tracers with roughly 134 reactions, respectively. The Kinetic PreProcessor (KPP) software version 2.2.3 (Damian et al., 2002;
36 Sandu and Sander, 2006) is employed to integrate the mCB05 gas-phase chemical mechanism for this work, based on the
37 generated Rosenbrock solver. A more detailed description and evaluation of the mCB05-KPP implementation can be found in
38 Myriokefalitakis et al. (2020).

39 Photodissociation rates were calculated inline using the Tropospheric Ultraviolet and Visible (TUV) Radiation model (Lee-
40 Taylor and Madronich, 2002). The TUV module calculates actinic flux and photolysis rates in each vertical layer within a 1-
41 D column of the Eulerian grid. The implemented wavelength grid ranges from 170-735 nm with 138 wavelength bins; 31
42 photodissociation reactions (out of 113 available in TUV) were selected for the implemented TUV module, covering all
43 relevant photolysis rates in the lower troposphere. Additionally, the model includes a light-dependent ground surface source
44 of nitrous acid (HONO) on top of the respective direct emissions from vehicles (Karl and Ramacher, 2021). In more detail, the
45 ground surface reaction producing HONO was parameterized according to Zhang et al. (2016) with a NO uptake coefficient
46 (γ) depending on the light intensity, i.e., when light intensity is less than 400 W m^{-2} a γ value of 2×10^{-5} is used;
47 otherwise, a factor of light intensity/400 is used to scale the γ value.

48 Pollutant concentrations in the sub-grid components (i.e., the Gaussian models for line and point source dispersion) are
49 determined by the EP10-Plume scheme, which contains 10 compounds and 17 reactions of O_3 , NO, NO_2 , HNO_3 , CO, and
50 formaldehyde (HCHO). In the line source sub-grid model, the simplified street canyon model (SSCM) is applied to calculate
51 pollutant dispersion in street canyons, and in the point source sub-grid model, the WMPP (WORM Meteorological Pre-
52 Processor) is integrated to calculate the wind speed at plume height. The rate of change of the concentrations of NO, NO_2 , and
53 O_3 in a street canyon is described in terms of chemical reaction, direct emissions, and background concentration. The mixing
54 processes are parameterized via the mixing time, which corresponds to the typical residence time of pollutants in a street
55 canyon. More details on the sub-grid photochemistry schemes of EPISODE-CityChem can be found in (Karl et al., 2019).

56 2.1.2 Extensions to the aerosol scheme

57 EPISODE-CityChem is extended for this work with online calculations of the main inorganic aerosol components, SO_4^{2-} , NO_3^- ,
58 NH_4^+ , in the presence of non-volatile cations from sea salt, dust, and domestic heating. For this, the aqueous-phase
59 formation of SO_4^{2-} in cloud droplets and the thermodynamic calculations, which determine the gas/particle partitioning of
60 $\text{NH}_3/\text{NH}_4^+$ and $\text{HNO}_3/\text{NO}_3^-$, are explicitly considered in the model. Aqueous phase oxidation of the dissolved SO_2 via H_2O_2
61 and O_3 in cloud droplets is added to the model. H_2O_2 produced in the gas phase can be rapidly dissolved in the liquid phase
62 due to its high solubility, and the dissolved H_2O_2 reacts rapidly with the HSO_3^- . Note that the dissociation of H_2O_2 is neglected
63 here. SO_2 oxidation in the aqueous phase is much faster than its gas phase homogeneous oxidation via OH radicals, with the
64 dissolved H_2O_2 being the most effective oxidant in the aqueous phase (Seinfeld and Pandis, 2006), especially when the solution
65 becomes acidic. At a higher pH ($\text{pH} > 4$), the dissolved SO_2 oxidation by ozone (O_3) tends to dominate the S(IV) oxidation,
66 even under dark conditions. Although laboratory studies have shown that dissolved SO_2 can also be oxidized in the presence
67 of transition metals via other pathways (Harris et al., 2013), such reactions are not currently considered in our model. Lastly,
68 the acidity of clouds is calculated using the electro-neutrality of strong acids (i.e., H_2SO_4 , SO_4^{2-} , HNO_3 , NO_3^-) and NH_4^+ , along
69 with the dissociations of CO_2 , SO_2 , and NH_3 . The reaction rates and the constants used to calculate the sulfur chemistry in the
70 model are presented in Table 1.

71 The ISORROPIA II thermodynamic equilibrium model (Fountoukis and Nenes, 2007) has been coupled to EPISODE-
72 CityChem to calculate the gas/particle partitioning of inorganic aerosols. ISORROPIA-II calculates the gas-liquid-solid
73 equilibrium partitioning of the K^+ - Ca^{2+} - Mg^{2+} - NH_4^+ - Na^+ - SO_4^{2-} - NO_3^- - Cl^- - H_2O aerosol system, and it is applied here
74 in the forward mode. NVCs from dust and sea salt aerosols are taken into account in the thermodynamic calculations considered
75 here as a fraction of $\text{PM}_{2.5}$ concentration. It is here assumed that constant mass ratios correspond to dust concentrations for
76 Ca^{2+} , Na^+ , K^+ , and Mg^{2+} of 1.2%, 1.5%, and 0.9%, respectively (Sposito, 1989). Accordingly, for sea spray aerosols, mean
77 mass fractions of 55.0% Cl^- , 30.6% Na^+ , 7.7% SO_4^{2-} , 3.7% Mg^{2+} , 1.2% Ca^{2+} , and 1.1% K^+ are applied (Seinfeld and Pandis,
78 2006).

79 Inorganic particles can be solid and/or composed of an aqueous supersaturated solution. The assumption of aqueous aerosol
80 for the acidity-sensitive semivolatile inorganic species (e.g., $\text{NH}_3/\text{NH}_4^+$ and $\text{HNO}_3/\text{NO}_3^-$) is found, though, to perform quite
81 well with a series of aerosol LWC observations when the relative humidity is above 40% (Bougiatioti et al., 2016; Guo et al.,
82 2015, 2017a). However, Cheng et al. (2022) recently indicated that although under high relative humidity conditions, both
83 assumptions may perform almost identically, the aqueous aerosol setup might perform better under high temperatures (>10
84 $^\circ\text{C}$) and low relative humidity ($<60\%$) conditions, while the solid aerosol setup might perform better for lower temperatures.
85 For this, the metastable aerosol setup is here applied for temperatures higher than $10\text{ }^\circ\text{C}$ and RH lower than 60% or higher than
86 83%. On the other hand, the stable aerosol setup is applied mostly at lower temperatures ($<5\text{ }^\circ\text{C}$). We note, however, that in
87 our case, there were only minimal differences (less than 1% in the simulated SIA concentrations during the cold period)
88 between simulations with only metastable (liquid) and variable aerosol state assumptions in thermodynamic calculations.

89 Even though this work is focused on the SIA fine aerosol fraction, nitrate aerosols are explicitly calculated for both the fine
90 and coarse modes (i.e., unlike SO_4^{2-} and NH_4^+). The rationale behind this is that nitrate is found to significantly contribute to
91 the coarse aerosol sizes (Koulouri et al., 2008), indicating that a bulk approach may lead to an overestimation of the $\text{HNO}_3/\text{NO}_3^-$
92 partitioning in the model, especially in areas with intense NVC contribution, such as from sea salt and dust aerosols, and from
93 anthropogenic combustion. For this practical application, kinetic limitations (Pringle et al., 2010) by mass transfer and transport
94 between the nitric acid in the gas phase and the particulate nitrate in $\text{PM}_{2.5}$ and PM_{10} are here considered, with ISORROPIA-
95 II then re-distributing the respective masses between the gas and the aerosol phases. We note, however, that the coarse nitrate
96 is not further taken into account in the thermodynamic calculations, assuming for simplicity that the gaseous HNO_3 , able to
97 condense in the coarse aerosol mode, partitions directly into the particulate bulk phase.

98 **2.1.3 Emissions**

99 Anthropogenic emissions were originally provided by the Copernicus Atmosphere Monitoring Service (CAMS). CAMS
100 provides the annual emission rates of CO , NH_3 , NMVOCs, NO_x , PM_{10} , $\text{PM}_{2.5}$, and SO_2 from the road, air, rail transport,
101 maritime (local and international shipping), mobile machinery, fuel production, industrial (paper, cement, minerals, metals,
102 etc.), stationary combustion, agriculture, waste, solvent use, and public power sectors. As evident, forest fires or biogenic
103 sources are not included in this dataset. CAMS adopts the GNFR sector classification and provides gridded data at 0.1×0.05
104 degrees. This dataset is then spatially refined over the domain of interest with the spatial disaggregation approach and tool
105 documented in Ramacher et al. (2021). In particular, the regional anthropogenic dataset is combined with GNFR-dependent
106 high-resolution spatial proxies (based on data from the European Pollutant and Transfer Register; E-PRTR, Global Human
107 Settlement Population; GHS-POP, Corine Land Cover; CLC, and OpenStreetMap; OSM) towards the spatial disaggregation
108 in $1 \times 1 \text{ km}^2$: i) area sources emitted 80 % in the model's layer 1 and 20 % in layer 2 for domestic heating, combustion in
109 manufacturing industry, agriculture and farming, and other mobile sources and machinery, except for shipping, where
110 emissions are equally distributed in the first 4 layers of the model; ii) point (industrial sources emitted at the height of each
111 stack); and iii) line emissions (road and railway emissions emitted at 0m). We note that the top heights of layers 1, 2, 3, and 4
112 are 17.5, 37.5, 62.5, and 87.5 m above the ground, respectively. Annual emissions are then converted into hourly emission
113 rates using monthly, weekly, and daily distributions based on average European factors, except for the yearly profiles for public
114 power, refineries, and road emissions, where CAMS-TEMPO factors are applied (Guevara et al., 2021). The respective maps
115 of the total annual emission fields are presented in Fig. S1.

116 Sea salt emissions are calculated for this work following the parameterizations from Gong (2003) and Vignati et al. (2010).
117 The flux of the number of sea-spray particles is expressed as a function of the particle radius at 80% humidity and the 10 m
118 horizontal wind speed, assuming number median dry radius values of 0.09 and $0.794 \mu\text{m}$ for fine and coarse sea-spray particles,
119 along with geometric standard deviations of 1.5 and 2.0, respectively (Vignati et al., 2010). To further address the temperature
120 effects on the sea spray source fluxes, polynomial expressions derived based on laboratory (chamber) experiments (Salter et

21 al., 2015) have been implemented. The total annual sea salt emissions, as calculated on-line by the model, are presented in the
22 supplement (Fig. S1e).

23 Potassium (K^+) emissions from anthropogenic wood-burning processes are further considered in our calculations, owing to
24 their significance for the thermodynamic equilibrium distribution of nitrogen-containing semivolatile compounds. For this, we
25 apply monthly factors to the $PM_{2.5}$ emissions from the domestic heating sector to derive the respective particle K^+ fluxes. The
26 non-sea salt $K^+/PM_{2.5}$ concentration ratios are derived from filter-based $PM_{2.5}$ measurements in the center of Athens
27 (Paraskevopoulou et al., 2014), specifically at the Thissio supersite (see Sect. 2.3). Assuming that in domestic wood
28 combustion episodes K^+ is directly emitted as part of the $PM_{2.5}$, an average fraction of 3.52% w/w contribution is here applied
29 to the respective $PM_{2.5}$ emissions for the winter months, as obtained by a positive matrix factorization (PMF) in central Athens
30 (Thissio) from December 2013 to March 2016 (Theodosi et al., 2018). SO_4^{2-} primary sources from residential combustion are
31 also accounted for in the model, owing to the significance of their ambient concentrations, accounting here for a fraction of
32 3.7% w/w (Zhang et al., 2023) of the $PM_{2.5}$ emitted during domestic wood combustion episodes. We note, however, that
33 although Zhang et al. (2023) indicate that NO_3^- and NH_4^+ can also be emitted from domestic combustion processes, the
34 respective emission factors are found to be 3–4 times lower compared to SO_4^{2-} , i.e., accounting for only up to 1% of the $PM_{2.5}$
35 emitted mass. For this reason, no primary emissions for NO_3^- , and NH_4^+ are accounted for in this study. The total annual K^+
36 emission field from anthropogenic wood-burning processes derived for this study is presented in Fig. S1f.

37 **2.1.4 Boundary conditions**

38 The CAMS European regional ensemble reanalysis data is used to create boundary conditions for O_3 , NO , NO_2 , CO , NH_3 ,
39 $PM_{2.5}$, PM_{10} , PAN, SO_2 , and NMVOC concentrations (chemically split to the species treated by the local model). Due to the
40 chemical advancements of the current work (SIA treatment), the CAMS global atmospheric composition forecast supports the
41 boundary conditions for H_2O_2 , N_2O_5 , HNO_3 , methacrolein/methyl vinyl ketone, N_2O_5 , HNO_3 , and HNO_4 , along with sea salt
42 aerosols in the fine and coarse sizes (not available on the regional scale). Furthermore, since the CAMS European regional
43 ensemble reanalysis data only provide SIA concentrations as lumped species, we also use the respective global atmospheric
44 composition forecast to derive the individual species (i.e., SO_4^{2-} , NO_3^- , and NH_4^+) normalized to the regional ensemble models'
45 SIA concentration data. The same assumption is applied for dust aerosols since dust concentrations are only provided as a part
46 of the PM_{10} fraction in the regional reanalysis data. NO_3^- in the coarse mode is directly derived from the global forecast data
47 (where available). The boundary conditions interface (BCONCAMS) developed at Helmholtz-Zentrum Hereon was utilized
48 for the interpolation of the CAMS regional ensemble and global forecast product and the mapping of the chemical species to
49 the urban air quality model. The interface performs bilinear interpolation in the horizontal and linear interpolation in the vertical
50 and projects the pollutant concentrations to the city domain. We note that several utilities allow the preparation of input files
51 or the conversion of these to the necessary CityChem input formats. More details on the utilities used to produce the EPISODE-
52 CityChem input files can be found in Karl et al. (2019).

53 **2.1.5 Meteorology**

54 The CTM EPISODE-CityChem is offline coupled with the mesoscale numerical weather prediction system Weather Research
55 and Forecasting (WRF). WRF is setup with Lambert-Conformal map projection, two-way nesting, Thompson graupel scheme
56 for microphysics, Monin-Obukhov (Janjic Eta) scheme for surface-layer parameterization, Noah Land-Surface model, and
57 Mellor-Yamada-Janjic (Eta) TKE scheme for boundary layer. The meteorological simulations are initialized by the synoptic-
58 scale meteorological reanalysis ensemble means (ECMWF ERA5). For this work, WRF is applied with a telescoping nesting
59 (3 domains), with the innermost domain covering the CTM area with a 1x1 km² spatial resolution. Hourly varying
60 meteorological variables used as inputs in the EPISODE-CityChem include pressure, air temperature, temperature gradient,
61 relative humidity, sensible and latent heat fluxes, total solar radiation, cloud fraction, and the cloud LWC.

62 **2.2 In-situ measurements**

63 In-situ aerosol chemical composition measurements conducted at 1) the Thissio Air Monitoring Supersite and 2) the Piraeus
64 monitoring station, both operated by the National Observatory of Athens, are here used to evaluate the model's ability to
65 simulate the main SIAs (SO₄²⁻, NH₄⁺, and NO₃) in the GAA, Greece. The Thissio Air Monitoring Supersite (37.9732° N,
66 23.7180° E, 105 m a.s.l.) is located on the premises of the National Observatory of Athens, in central Athens. The site is far
67 from major traffic roads, in a moderately populated residential area, and thus is considered representative of urban background
68 conditions in the center of the Athens basin (Grivas et al., 2019; Panopoulou et al., 2020), as it serves as a receptor of pollutants
69 from different sources and with various degrees of processing. Online measurements took place throughout 2019 at Thissio,
70 apart from the period when the instrumentation for online aerosol SIA measurements was moved to the Piraeus site.
71 Measurements were conducted at a central location during two periods in winter (10 December 2018 - 16 January 2019) and
72 summer (11 June 2019 - 9 July 2019). The instruments in Piraeus were located on the 1st floor (9m above ground) of the
73 Athens Metro terminal station building (Urban Rail Transport S.A., Athens, Greece; 37.9479° N, 23.6429° E, 10 m a.s.l.). The
74 site is influenced to an extent by traffic emissions, being at a distance of 70 m from the coastal avenue in the Piraeus port area
75 (Stavroulas et al., 2021).

76 High-temporal resolution measurements of non-refractory submicron aerosol chemical composition at both sites were
77 performed with a quadrupole Aerosol Chemical Speciation Monitor (ACSM; Aerodyne Research Inc.; Ng et al., 2011),
78 operated at a 30-minute temporal resolution. The instrument provides concentrations of ammonium, sulfate, nitrate, chloride,
79 and organic matter. Details on the limits of detection, sampling, and calibration of the instrument can be found in Stavroulas
80 et al. (2019, 2021). QA/QC of ACSM measurements included the comparison of the daily-averaged online and offline
81 measurements. The estimation of sea salt, non-sea salt potassium, and dust was performed using the methodology of Sciare et
82 al. (2005). Although the evaluation of dust concentrations is out of the scope of this study, we note that the estimation of
83 atmospheric dust levels using the calcium ion as a proxy (Sciare et al., 2005) may be largely uncertain due to major
84 contributions from other sources. It should also be noted that since ion chromatography quantifies mostly the inorganic

85 components, it is expected that interferences may occur for sulfate and nitrate, especially during winter, when nitrites, organic
86 nitrates, and sulfates are variably present (Guo et al., 2016).

87 **3 Results and discussion**

88 **3.1 Model evaluation**

89 **3.1.1 Sulfate**

90 Observations indicate that the hourly SO_4^{2-} concentrations present only a slightly increasing trend from winter to summer 2019
91 over Athens (Fig. 2a). During the warm season, however, the scarcity or absence of precipitation in the region, along with
92 increased transport through the boundaries and mostly the higher oxidation potential, resulted in an overall increase in SO_4^{2-}
93 concentrations in the model (W/ SIA), although still lower compared to observations. The enhanced summer concentrations
94 in the model are nonetheless in accordance with previous observational and modeling studies in the area (Athanasopoulou et
95 al., 2015; Grivas et al., 2018; Paraskevopoulou et al., 2015; Theodosi et al., 2018), suggesting that the majority of SO_4^{2-} mainly
96 originates from long-range transport (e.g., Balkan countries and the wider Black Sea region) due to fossil fuel combustion in
97 power production and other industrial plants (Aksoyoglu et al., 2017). This is also clearly shown by the present sensitivity
98 model calculations, indicating that when the local SO_4^{2-} production via aqueous-phase SO_2 oxidation is neglected (W/O SIA),
99 the simulated SO_4^{2-} concentrations remain practically unchanged in most of the cases, especially during the warm periods.
00 EPISODE-CityChem captures the observed hourly SO_4^{2-} surface levels in Piraeus and Thissio, with a correlation coefficient
01 (r) of 0.46 and an annual mean bias of $-1.2 \mu\text{g m}^{-3}$ (Fig. 2a), partly attributed to the temporal variation of emissions, which is
02 largely based on Europe-wide factors provided along with the CAMS-REG yearly data. The model tends to overall
03 underestimate the observations, presenting for 2019 a negative normalized mean bias (nMB) of -42%. Our simulations
04 nevertheless indicate that the underestimation of the modeled SO_4^{2-} concentrations should be mainly due to the too low long-
05 range transport in the area through the boundaries, since only a weak local SO_4^{2-} formation is supported by the model. Indeed,
06 when comparing the base simulation (W/ SIA) with the W/O SIA sensitivity simulation, where the local SO_4^{2-} production in
07 cloud droplets is neglected, only a slight increase in the surface SO_4^{2-} concentrations is illustrated, without any noteworthy
08 change ($< 1\%$) in the respective correlation statistics. On the other hand, the underrepresentation of SO_x ($= \text{SO}_2 + \text{SO}_4^{2-}$) local
09 emissions, or even a too slow SO_2 oxidation in the gas phase, could further contribute to the model's underestimation of the
10 observed values. Last, although WRF accurately predicts temperature and humidity fields, it tends to overestimate wind speed
11 (see Table S1 in the Supplement). This has the effect of enhanced ventilation and dispersion of SO_4^{2-} (and the rest of SIAs),
12 which may partially explain the observed negative biases in the simulated pollutants under study.

13 3.1.2 Nitrate

14 The observed and modeled NO_3^- concentrations increase during the cold period (Fig. 2b), presenting a pronounced seasonality.
15 The increase mentioned above is caused by both the formation of NH_4NO_3 under low ambient temperatures (Theodosi et al.,
16 2018) and the presence of non-volatile potassium cations from domestic heating processes, which can significantly promote
17 the formation of KNO_3 . On the contrary, the observed NO_3^- concentrations are considerably reduced in summer (Liakakou et
18 al., 2022; Paraskevopoulou et al., 2015), owing to the thermal instability and volatilization of the NH_4NO_3 .

19 Sensitivity model simulations clearly indicate that NO_3^- is a local pollutant rather than a transported one in the GAA. This
20 agrees with previous modeling studies where road traffic is found to significantly contribute to NO_3^- in eastern Europe
21 (Aksoyoglu et al., 2017). Indeed, when the thermodynamics are neglected in model calculations (W/O SIA), NO_3^-
22 concentrations are severely underestimated over GAA in almost all seasons of the year, except for some cases during the
23 summer months (July and, to a lesser extent, August). Although EPISODE-CityChem tends to calculate very low NO_3^- levels
24 during the warm period for the base simulation (W/ SIA), the maxima during July and August due to the contribution of long-
25 range transport from biomass burning processes (such as wildfires in Attica and the island of Evia in July and August 2019)
26 seem not to be well captured by the model. On the other hand, the W/O Kbb sensitivity model simulation clearly indicates that
27 the presence of K^+ associated with domestic heating processes plays a crucial role in NO_3^- formation during the winter period,
28 leading overall to a lower nMB compared to the base simulation (i.e., -63% vs. -61%). This, yet, is in accordance with previous
29 findings in the region, where a good correlation between K^+ with OC, EC, and NO_3^- has been observed during winter (Fourtziou
30 et al., 2017; Theodosi et al., 2018), thus clearly supporting their common origin during the cold period. In more detail,
31 residential biomass burning processes are found to be directly responsible for the winter maxima measured over GAA, while
32 intense Saharan dust episodes under the local southerly winds may also have an impact on the spring peak.

33 A better correlation compared to that of SO_4^{2-} is found when comparing the model and the measurements for the hourly NO_3^-
34 surface levels ($r = 0.58$). The model, however, tends to overall underestimate the observations, with a slightly negative bias of
35 around $-0.4 \mu\text{g m}^{-3}$ and an nMB of roughly -61% for the year 2019, mainly due to the too low summertime simulated
36 concentrations (Fig. 2b). We note, nevertheless, that an underestimation of the observed concentrations is here expected since,
37 on the one hand, some ammonia sources, such as from agricultural soils, are currently omitted in the model, and on the other
38 hand, species that may be accounted for in the observational data, such as nitrites and organic nitrates that may also be present
39 during winter and partition in the particulate phase (Guo et al., 2016), are not yet included in the presented chemical
40 mechanism. Still, correlation statistics clearly denote that the local HNO_3 partitioning in the particulate phase is the main
41 pathway of fine particulate NO_3^- formation in the study area, and more specifically, that the presence of K^+ , either from
42 domestic burning processes or dust events, plays a crucial role in the NO_3^- concentration distributions.

43 3.1.3 Ammonium

44 The observed NH_4^+ concentrations (Fig. 2c) generally present a similar seasonal pattern to that of SO_4^{2-} , although somehow
45 with a more intense trend during the warm season. As already found in previous works (Mantas et al., 2014; Paraskevopoulou
46 et al., 2015; Theodosi et al., 2018), observations of NH_4^+ and SO_4^{2-} are highly correlated ($r = 0.79$) indicating that nss- SO_4^{2-}
47 can be considered at least partially neutralized by NH_4^+ . The simulated sulfate/ammonium ratio for the base simulation ($r =$
48 0.73) shows that sulfate exists mainly in the model in the form of NH_4HSO_4 and $(\text{NH}_4)_2\text{SO}_4$ in the two sites (i.e., Thissio and
49 Piraeus), in agreement with previous studies in the wider eastern Mediterranean area (Athanasopoulou et al., 2008; Bardouki
50 et al., 2003; Fourtziou et al., 2017; Koulouri et al., 2008). Nevertheless, during the cold season, NH_4^+ is also found to be
51 significantly correlated with NO_3^- ($r = 0.62$), indicative of NH_4NO_3 formation, respectively. Note, however, that for this work,
52 the non-sea salt chloride is not considered in model calculations, so the nss- NH_4Cl does not contribute to the calculated NH_4
53 concentrations.

54 The base case simulation of EPISODE-CityChem captures the observed NH_4^+ hourly surface observations in Piraeus and
55 Thissio with a correlation coefficient (r) of 0.57 and a negative mean bias of $-0.4 \mu\text{g m}^{-3}$ (Fig. 2f), with a calculated negative
56 nMB of -46% for 2019. However, when the thermodynamic calculations are neglected in the model in the W/O SIA simulation
57 (i.e., accounting only for the transport from the model's boundaries contributing to the NH_4^+ levels), the agreement tends to
58 improve, leading to a correlation coefficient (r) of 0.61, a negative mean bias of $-0.2 \mu\text{g m}^{-3}$, and a negative nMB of -22% (Fig.
59 2f). This can be explained due to the volatilization of NH_4^+ for the base simulation when thermodynamics are taken into
60 account in the model, which overall shifts NH_4^+ to gas-phase NH_3 (Guo et al., 2018).

61 The significance of aerosol pH levels on NH_4^+ volatilization is further supported by the model sensitivity simulation when the
62 contribution of K^+ from domestic heating processes is neglected in the thermodynamic calculations (W/O Kbb). Indeed, the
63 absence of K^+ increases the acidity in the aerosol phase and thus enhances the gas/particle partitioning of $\text{NH}_3/\text{NH}_4^+$. Overall,
64 the improved correlation of model results with observations in the absence of K^+ from domestic heating compared to the base
65 case simulation (i.e., $r = 0.61$, bias = -0.3 , and nMB = -37%) indicates that the model misses primary NH_3 emissions from
66 sources like road transport, that could contribute up to 10% to NH_4^+ ambient levels (Aksoyoglu et al., 2017), or from non-
67 urban sources, such as the volatilization of animal waste and synthetic fertilizers, biomass combustion, and losses from natural
68 soils (e.g., Fameli and Assimakopoulos, 2016)

69 3.2 Spatial model concentration fields

70 The mapping of the main SIAs at ground level, as simulated by EPISODE-CityChem averaged for the winter (January,
71 February, and December 2019) and summer (June, July, and August 2019) periods, is presented in Fig. 3. Additionally, the
72 spatio-temporal totals of the SIA-related tracer emissions are presented in Fig. S2. During both seasons, high SO_4^{2-} levels are
73 simulated near the major emission hotspots, such as shipping routes around the Ports of Piraeus and Eleusis and large
74 combustion plants in the Thriassion Plain (Fig. 1), where the vast majority of the surface SO_2 emissions in the GAA occur.

75 During summer (Fig. 3b), the predicted SO_4^{2-} surface concentrations are close to $2.86 \pm 0.92 \mu\text{g m}^{-3}$ in the center of Athens
76 and the suburbs, while during winter (Fig. 3a) the season mean simulated concentrations vary between 1.31 and $4.45 \mu\text{g m}^{-3}$.
77 The results indicate that long-range transport is an important contributor to SO_4^{2-} surface concentrations in the area, which are
78 maximized during the summer due to enhanced photochemical activity. On average, SO_4^{2-} is calculated to have an annual
79 mean surface concentration of $2.15 \pm 0.88 \mu\text{g m}^{-3}$ for the year 2019 in the model domain. Sensitivity model calculations
80 confirmed this, showing that chemical production in the model domain can support up to 10% of the wintertime SO_4^{2-} surface
81 concentrations (Fig. 4a), mainly in higher altitude areas, such as Parnitha Mt. (Fig. 1), where cloudiness is enhanced and the
82 increased cloud LWC promotes the aqueous phase oxidation of ambient SO_2 . Around the city center, however, the chemical
83 formation contribution to the surface SO_4^{2-} levels is calculated to be rather low (roughly 4%).

84 The average fine NO_3^- concentrations in the model are calculated to vary between 0.05 and $1.50 \mu\text{g m}^{-3}$ during the cold period
85 (Fig. 3c). A mean NO_3^- concentration of $0.51 \pm 0.20 \mu\text{g m}^{-3}$ is simulated during the winter months, while only $0.05 \pm 0.05 \mu\text{g}$
86 m^{-3} is calculated during the summer (Fig. 3d). In the model domain, NO_3^- registered an annual mean surface concentration of
87 $0.24 \pm 0.23 \mu\text{g m}^{-3}$ for 2019. In contrast, however, to the SO_4^{2-} surface concentrations, NO_3^- levels present notable spatial
88 variability, with much higher concentrations calculated near rather than away from the city center during the winter, compared
89 to the negligible concentrations in the warm season. This indicates that NO_3^- formation significantly depends on the local
90 meteorological conditions (i.e., temperature and relative humidity) along with the anthropogenic emissions of precursor species
91 that are widespread in the GAA (Fig. 1), mainly from traffic, and especially the presence of NVCs such as K^+ from domestic
92 heating in winter that can support an increase in NO_3^- surface concentrations of about $10 \pm 4\%$ in the model domain (Fig. 4d).
93 It is noted that in this study, NO_3^- is only either formed in the model domain as a secondary product or transported from the
94 boundaries, without any primary contribution. However, the enhanced concentrations around the city center in the model
95 clearly indicate that NO_3^- is mainly a local pollutant rather than a transported one over the GAA. The latter is further supported
96 through sensitivity model calculations performed for this work, demonstrating that when thermodynamics are accounted for
97 in the model (Fig. 4c), more than 80% of the NO_3^- surface concentrations on an annual basis in downtown Athens (Fig. 1) are
98 directly attributed to the HNO_3 gas/particle partitioning.

99 The average surface NH_4^+ concentrations in the model are calculated to be without strong annual variability in the GAA for
00 2019. For the cold period (Fig. 3e), the model simulates that NH_4^+ concentration varies between 0.30 in the suburbs and 1.40
01 $\mu\text{g m}^{-3}$ around the city center, while for the summertime it is between 0.33 and $1.18 \mu\text{g m}^{-3}$, respectively (Fig. 3f). For the year
02 2019, NH_4^+ is calculated to have an annual mean surface concentration of $0.58 \pm 0.14 \mu\text{g m}^{-3}$ in the model domain. Model
03 simulations show that the available anthropogenic NH_3 emissions in the model domain tend to quickly neutralize the primary
04 strong acids present in the urban atmosphere of Athens, like H_2SO_4 and HNO_3 , which subsequently partition into the aerosol
05 aqueous phase in the form of the ammonium ion. As already discussed in Sect. 3.1.3, when thermodynamics are included in
06 model simulation, an increase in volatilization of NH_4^+ is calculated that, on an annual basis, can support a decrease in its
07 concentrations up to 70% in the suburbs (Fig. 4e). On the other hand, much lower NH_4^+ volatilization is calculated around the
08 Thriassion Plain, where combustion plants exist, as well as in the region's major port zones (Fig. 1), due to primary NH_3

09 sources. The latter indicates that although traffic, solid and water waste management facilities, and certain industrial processes
10 (e.g., refineries, cement manufacturing, livestock production) seem to be the main NH_3 sources in urban areas (Liakakou et al.,
11 2023), ammonia may also be strongly related to agricultural activities and soil sources in rural areas, which in turn significantly
12 impacts NH_4^+ concentrations; however, NH_3 emissions from such sectors are not currently included in our model. Additionally,
13 emissions from domestic heating may also have some impact on NH_3 surface levels (Fig. 4f), since in the presence of non-
14 volatile potassium cation such as from biomass burning processes, the formation of KNO_3 is promoted and thus the gas/particle
15 partitioning of NH_3 is reduced ($12 \pm 2\%$).

16 **3.3 Atmospheric water and acidity**

17 Particle LWC and aerosol pH are important parameters of the aerosol phase; however, limited in situ observations of aerosol
18 pH exist due to the non-conserved nature of H^+ and the dissociation of inorganic and organic electrolytes in the particulate
19 phase. Since ion balance proxy methods generally lead to miscalculations of aerosol acidity levels, thermodynamic model
20 calculations can be considered a reliable tool for such calculations (Hennigan et al., 2015). The acidity levels in an urban
21 environment are primarily governed by the atmospheric LWC and the aqueous-phase proton concentration ($[\text{H}^+]$). The impacts
22 of cloud LWC and aerosol water on atmospheric acidity significantly differ; cloud liquid water is primarily determined by
23 meteorological conditions, while aerosol water is subject to chemical equilibrium with atmospheric water vapors. Thus, the
24 hygroscopicity of the dissolved aerosol species plays a significant role in governing the aerosol water content under specific
25 relative humidity levels (Pye et al., 2020). Moreover, the pH levels in clouds are found to be notably higher (up to four units;
26 Seinfeld and Pandis, 2006) in comparison to aerosols, owing to the dilute conditions prevailing in them. On the contrary,
27 aerosol acidity is determined not only by the equilibrium between acidic and alkaline species but also by the relative
28 concentrations of such species that partition in the particulate phase under favorable temperature and relative humidity
29 conditions (Pye et al., 2020).

30 Figure 5 illustrates the averaged pH levels of fine aerosols and the respective particulate water content on the surface for winter
31 and summer, as calculated by EPISODE-CityChem. The calculated pH for fine aerosols over the GAA can be rather acidic,
32 with an average value of 4.81 ± 0.93 during winter (Fig. 5a) and 2.20 ± 1.00 during summer (Fig. 5b), varying spatially between
33 2.38 - 7.58 and 0.79 - 5.82, respectively. Minimum pH values are calculated to differ by roughly one unit, indicating an overall
34 10-fold increase in the aerosol H^+/LWC ratio from summer to winter periods in the model. Such a variation in the aerosol
35 acidity can be directly attributed to the significantly different meteorological parameters between the two seasons, illustrating
36 the importance of the increased relative humidity levels on aerosol pH values during the cold period. Nonetheless, the
37 persistence of strong acidity in fine aerosols can also be attributed to the thermodynamic equilibrium between NH_4^+ and NH_3
38 that overall promotes the NH_x ($= \text{NH}_3 + \text{NH}_4^+$) volatilization in the model. This is in accordance with other studies where,
39 although gaseous NH_3 may be abundant, the pH values of $\text{PM}_{2.5}$ remain acidic (Ding et al., 2019). Note, however, that for this
40 study we only account for the water associated with the inorganic aerosol component; thus, the model may slightly
41 underestimate the particulate water by 0.15-0.23 units compared to the pH predicted with total water (Guo et al., 2015). This

42 value is likely an upper bound on the error since organic aerosol mass fractions in the specific location were high (~60%; Guo
43 et al., 2015; Stavroulas et al., 2019). On the other hand, the significantly higher maximum pH values during wintertime cannot
44 be only attributed to meteorology. In accordance with previous studies, higher aerosol pH levels can be directly associated
45 with the presence of NVCs emanating from wood-burning processes (Bougiatioti et al., 2016; Zhang et al., 2015). For
46 completeness, the calculated surface aerosol water concentrations for winter (Fig. 5c) and summer (Fig. 5d) are also provided.
47 The long-range transport of SIA along with the emissions of its precursors, such as SO₂ and NO_x, tend to also decrease local
48 cloud pH levels in the model. It should be mentioned that EPISODE-CityChem does not calculate, but instead only reads the
49 cloud LWC and the cloud cover from meteorological files in the region, meaning that no transport of clouds exists in the model
50 domain. During the winter season (Fig. 5e), higher cloud pH values have been generally calculated as compared to the summer
51 season (not shown). The cloud pH is calculated to vary between 3.50 and 6.70 during the wintertime over Athens, mostly in
52 the suburbs where the higher cloudiness exists, owing to the orography of the regions. On the contrary, during the summer,
53 the model calculates clouds of higher acidity (i.e., up to ~0.28 pH units). This, however, can be attributed mainly to the relative
54 absence of cloud water during the warm period in the model, along with the increased transport of acidic compounds like
55 sulfates (i.e., very concentrated solutions lead to strongly acidic pH values). Note, however, that the potential impact of mineral
56 dust, particularly calcium, on cloud H⁺ concentrations has been neglected in the above calculations. Such an assumption could
57 potentially lead to an overestimation of cloud acidity, especially during the dust event periods (mainly late winter and spring).
58 A further constraint in the assessment of cloud acidity pertains to the exclusion of low-molecular-weight organic acids (e.g.,
59 formic and acetic acids), which may also result in some degree of miscalculation of the cloud acidity levels.

60 **4 Summary and conclusions**

61 For this work, the ISORROPIA II thermodynamic model has been coupled to the urban-scale EPISODE-CityChem CTM to
62 calculate the gas/particle partitioning of NH₃/NH₄⁺ and HNO₃/NO₃⁻, providing insights into complex interactions in a major
63 Eastern Mediterranean urban agglomeration. While the model tends to generally underestimate the SIA measurements over
64 the Greater Area of Athens, it tracks their observed daily variation at Piraeus and Thissio monitoring stations. SIA formation
65 appears to significantly depend on the ambient precursor gasses (SO₂, NO_x, and NH₃), which represent an important fraction
66 (i.e., up to 20% during both cold and warm periods) of PM_{2.5} in the model domain, especially in suburban areas. Nevertheless,
67 long-range transport is found to be a critical factor in determining the SIA ambient concentrations, especially for SO₄²⁻. Indeed,
68 the model's underestimation of observed SO₄²⁻ concentrations rather indicates a too weak transport from the boundaries than a
69 too low secondary formation from primary SO_x sources. Respectively, the lower NH₄⁺ concentrations compared to the observed
70 values generally follow the variations of the simulated SO₄²⁻, as also denoted by the derived sulfate/ammonium ratio, where
71 sulfate is mainly in the form of NH₄HSO₄ and (NH₄)₂SO₄. Specifically, during the cold period, the relatively basic aerosol pH
72 values enhance the volatilization of NH₄⁺ in the model, and along with possibly missing NH₃ sources, the model tends to
73 underestimate the measurements.

74 The inclusion of non-volatile cations originated from biomass burning sources, along with sea salt and dust aerosols, has
75 nevertheless had a critical impact on the ion balance and thus the partitioning of semi-volatile compounds (i.e., nitrate and
76 ammonium) in the model. Although this study is focused on the fine PM fraction, we note that high nitrate concentrations have
77 been found to be well correlated with increased concentrations of super-micron dust and sea spray particles (Allen et al., 2015),
78 indicating the importance of crustal species in the $\text{HNO}_3/\text{NO}_3^-$ partitioning. Still, besides the presence of sea salt and dust
79 aerosols, the inclusion of K^+ from domestic wood-burning combustion sources in the aerosol thermodynamic calculations is
80 found to affect the ion balance and thus the formation of NO_3^- , due to a more effective partitioning in the aerosol phase during
81 the cold and humid conditions. NO_3^- concentrations for 2019 exhibit a relatively lower value in comparison to the observations,
82 with a correlation coefficient of 0.58 and a normalized mean bias of -61%. However, the model performs better in simulating
83 NO_3^- concentrations as compared to SO_4^{2-} (i.e., $r = 0.46$) and NH_4^+ (i.e., $r = 0.57$), suggesting a satisfactory representation of
84 the $\text{HNO}_3/\text{NO}_3^-$ partitioning. On the other hand, the volatilization of NH_4^+ due to a decrease in aerosol pH (especially during
85 the warm period) tends to shift NH_4^+ to the gas-phase, further indicating missing NH_3 sources in the model.

86 It is well established that SIAs play an important role in urban air quality and can have detrimental effects on the environment
87 and human health. Thus, reducing emissions of their precursors via measures including, inter alia, the extensive use of
88 sustainable energy, mobility, and agriculture is crucial for mitigating such effects in the long term. The continuation of such
89 policies on the European level appears critical, especially in view of new air quality management legislation in the EU that
90 will set very ambitious PM standards for the protection of public health, which will be difficult to attain unless sweeping
91 emission cutbacks are implemented. Moreover, despite the fact that the reduction in primary pollutants like SO_2 and NO_x can
92 also reduce the acidity of cloud water and precipitation (Watmough et al., 2016), fine aerosols may still remain highly acidic
93 in a future atmosphere due to the respective NH_3 volatilization in the particulate phase (Baker et al., 2021; Lawal et al., 2018).
94 On the other hand, it is shown here that, accounting for the K^+ sources from domestic wood burning in the model, significantly
95 higher aerosol pH values can be locally supported during the winter compared to the warm period, where K^+ is mostly
96 associated with Saharan dust outbreaks in the GAA (Theodosi et al., 2018). Nevertheless, such a discrepancy in the response
97 of the fine aerosol pH to emission controls also has noteworthy implications for the toxicity of atmospheric particles, especially
98 during the cold period where domestic wood burning may consist of an additional source of harmful air pollution. Such
99 complex chemical interactions have not yet, however, been comprehensively acknowledged in urban-scale studies (Zhang et
00 al., 2022).

01 In this study, the high spatiotemporal resolution of EPISODE-CityChem (up to $100 \times 100 \text{ m}^2$, 1 h) with the improved
02 representation of the inorganic aerosols delivers a beyond-the-state-of-the-art characterization of the fine particulate load over
03 the GAA. Focusing further on air-quality studies in polluted urban domains, several initiatives are underway aimed at
04 improving EPISODE-CityChem's modeling of aerosols and the respective chemical processes. These include coupling with
05 aerosol microphysical schemes that will account for new particle formation and aerosol aging through coalescence and
06 condensation (e.g., Karl et al., 2023). Such developments aim to improve the model's ability to represent the composition and
07 size distribution of fine PM. A better characterization of aerosol chemical speciation, like the consideration of organic aerosols,

08 is expected to also improve the aerosol hygroscopicity calculations in the model, especially within the boundary layer where
09 the contribution of water-soluble organics to total aerosol mass is important (i.e., Bougiatioti et al., 2016). The KPP software
10 for solving stiff numerical systems has already been coupled to the model to integrate the gas phase photochemistry schemes,
11 and based on this development, more explicit chemical schemes are planned to be available in the model. Furthermore, gas-
12 phase organic species can also be oxidized in the interstitial cloud space and form water-soluble compounds like aldehydes,
13 which rapidly partition into droplets. In the presence of oxidants (e.g., OH and NO₃ radicals), the dissolved organics can also
14 undergo chemical conversions and form low-volatile organics that remain partially in the aerosol phase. A state-of-the-art
15 multiphase chemical scheme (e.g., Myriokefalitakis et al., 2022) is therefore planned to be coupled to the model to account for
16 such an aerosol formation process in an urban area. Additionally, parameterizations of marine dimethylsulfide (DMS) and
17 organic aerosol primary sources in the model are currently under consideration.

18 The proposed model framework, coupled with emission reduction scenarios, may enable a thorough investigation of the
19 regulations and interventions that can efficiently curtail air pollution in the GAA and, consequently, its health impacts,
20 providing a valuable decision support tool to the air quality management authorities in view of the realignment with the new
21 air quality standards that will be inevitable in the near future, given the present state of air quality in Greece. Anticipated
22 advancements in model parallelization and code architecture are expected to facilitate computationally efficient urban
23 simulations and the creation of state-of-the-art forecasting systems capable of generating high-resolution air quality predictions
24 for multiple urban regions in Europe up to street level. Overall, providing such an urban-scale modeling tool allows for a more
25 accurate articulation of strategies for air quality management, including the optimization of monitoring protocols as well as
26 the mitigation of emissions from various activity sectors and adverse effects.

- 29 Aksoyoglu, S., Ciarelli, G., El-Haddad, I., Baltensperger, U., and Prévôt, A. S. H.: Secondary inorganic aerosols in Europe:
30 sources and the significant influence of biogenic VOC emissions, especially on ammonium nitrate, *Atmospheric Chemistry
31 and Physics*, 17, 7757–7773, <https://doi.org/10.5194/acp-17-7757-2017>, 2017.
- 32 Alexander, B., Park, R. J., Jacob, D. J., and Gong, S.: Transition metal-catalyzed oxidation of atmospheric sulfur: Global
33 implications for the sulfur budget, *Journal of Geophysical Research*, 114, D02309, <https://doi.org/10.1029/2008JD010486>,
34 2009.
- 35 Allen, H. M., Draper, D. C., Ayres, B. R., Ault, A., Bondy, A., Takahama, S., Modini, R. L., Baumann, K., Edgerton, E.,
36 Knote, C., Laskin, A., Wang, B., and Fry, J. L.: Influence of crustal dust and sea spray supermicron particle concentrations
37 and acidity on inorganic
38 NO₃ aerosol
39 during the 2013 Southern Oxidant and Aerosol Study, *Atmospheric Chemistry and Physics*, 15, 10669–10685,
40 <https://doi.org/10.5194/acp-15-10669-2015>, 2015.
- 41 Athanasopoulou, E., Tombrou, M., Pandis, S. N., and Russell, A. G.: The role of sea-salt emissions and heterogeneous
42 chemistry in the air quality of polluted coastal areas, *Atmospheric Chemistry and Physics*, 8, 5755–5769,
43 <https://doi.org/10.5194/acp-8-5755-2008>, 2008.
- 44 Athanasopoulou, E., Vogel, H., Vogel, B., Tsimpidi, A. P., Pandis, S. N., Knote, C., and Fountoukis, C.: Modeling the
45 meteorological and chemical effects of secondary organic aerosols during an EUCAARI campaign, *Atmospheric Chemistry
46 and Physics*, 13, 625–645, <https://doi.org/10.5194/acp-13-625-2013>, 2013.
- 47 Athanasopoulou, E., Protonotariou, A. P., Bossioli, E., Dandou, A., Tombrou, M., Allan, J. D., Coe, H., Mihalopoulos, N.,
48 Kalogiros, J., Bacak, A., Sciare, J., and Biskos, G.: Aerosol chemistry above an extended archipelago of the eastern
49 Mediterranean basin during strong northern winds, *Atmospheric Chemistry and Physics*, 15, 8401–8421,
50 <https://doi.org/10.5194/acp-15-8401-2015>, 2015.
- 51 Athanasopoulou, E., Protonotariou, A., Papangelis, G., Tombrou, M., Mihalopoulos, N., and Gerasopoulos, E.: Long-range
52 transport of Saharan dust and chemical transformations over the Eastern Mediterranean, *Atmospheric Environment*, 140,
53 592–604, <https://doi.org/10.1016/j.atmosenv.2016.06.041>, 2016.
- 54 Atkinson, R., Baulch, D. L., Cox, R. A., Crowley, J. N., Hampson, R. F., Hynes, R. G., Jenkin, M. E., Rossi, M. J., and Troe,
55 J.: Evaluated kinetic and photochemical data for atmospheric chemistry: Volume I - gas phase reactions of Ox, HOx, NOx
56 and SOx species, *Atmospheric Chemistry and Physics*, 4, 1461–1738, <https://doi.org/10.5194/acp-4-1461-2004>, 2004.
- 57 Baker, A. R., Kanakidou, M., Nenes, A., Myriokefalitakis, S., Croot, P. L., Duce, R. A., Gao, Y., Guieu, C., Ito, A., Jickells,
58 T. D., Mahowald, N. M., Middag, R., Perron, M. M. G., Sarin, M. M., Shelley, R., and Turner, D. R.: Changing atmospheric
59 acidity as a modulator of nutrient deposition and ocean biogeochemistry, *Science Advances*, 7, eabd8800,
60 <https://doi.org/10.1126/sciadv.abd8800>, 2021.
- 61 Bardouki, H., Liakakou, H., Economou, C., Sciare, J., Smolík, J., Ždímal, V., Eleftheriadis, K., Lazaridis, M., Dye, C., and
62 Mihalopoulos, N.: Chemical composition of size-resolved atmospheric aerosols in the eastern Mediterranean during summer
63 and winter, *Atmospheric Environment*, 37, 195–208, [https://doi.org/10.1016/S1352-2310\(02\)00859-2](https://doi.org/10.1016/S1352-2310(02)00859-2), 2003.
- 64 Basagaña, X., Jacquemin, B., Karanasiou, A., Ostro, B., Querol, X., Agis, D., Alessandrini, E., Alguacil, J., Artiñano, B.,
65 Catrambone, M., De La Rosa, J. D., Diaz, J., Faustini, A., Ferrari, S., Forastiere, F., Katsouyanni, K., Linares, C., Perrino,
66 C., Ranzi, A., Ricciardelli, I., Samoli, E., Zauli-Sajani, S., Sunyer, J., and Stafoggia, M.: Short-term effects of particulate
67 matter constituents on daily hospitalizations and mortality in five South-European cities: Results from the MED-
68 PARTICLES project, *Environment International*, 75, 151–158, <https://doi.org/10.1016/j.envint.2014.11.011>, 2015.
- 69 Basla, B., Agresti, V., Balzarini, A., Giani, P., Pirovano, G., Gilardoni, S., Paglione, M., Colombi, C., Belis, C. A., Poluzzi,
70 V., Scotto, F., and Lonati, G.: Simulations of Organic Aerosol with CAMx over the Po Valley during the Summer Season,
71 *Atmosphere*, 13, 1996, <https://doi.org/10.3390/atmos13121996>, 2022.
- 72 Bougiatioti, A., Nikolaou, P., Stavroulas, I., Kouvarakis, G., Weber, R., Nenes, A., Kanakidou, M., and Mihalopoulos, N.:
73 Particle water and pH in the eastern Mediterranean: source variability and implications for nutrient availability, *Atmospheric
74 Chemistry and Physics*, 16, 4579–4591, <https://doi.org/10.5194/acp-16-4579-2016>, 2016.
- 75 Brandt, F., Bosbach, D., Krawczyk-Barsch, E., Arnold, T., and Bernhard, G.: Chlorite dissolution in the acid pH-range: a

76 combined microscopic and macroscopic approach, *Geochimica et Cosmochimica Acta*, 67, 1451–1461,
77 [https://doi.org/10.1016/S0016-7037\(02\)01293-0](https://doi.org/10.1016/S0016-7037(02)01293-0), 2003.

78 Cheng, B., Wang-Li, L., Classen, J., and Bloomfield, P.: Performance of a Thermodynamic Model for Predicting Inorganic
79 Aerosols in the Southeastern U.S., *Atmosphere*, 13, 1977, <https://doi.org/10.3390/atmos13121977>, 2022.

80 Clegg, S. L., Brimblecombe, P., and Wexler, A. S.: **Thermodynamic Model of the System**
81 **$H^+ - NH_4^+ - SO_4^{2-} - NO_3^- - H_2O$ at Tropospheric Temperatures**, *J. Phys. Chem. A*, 102, 2137–
82 2154, <https://doi.org/10.1021/jp973042r>, 1998.

83 Damian, V., Sandu, A., Damian, M., Potra, F., and Carmichael, G. R.: The kinetic preprocessor KPP—a software environment
84 for solving chemical kinetics, *Computers & Chemical Engineering*, 26, 1567–1579, [https://doi.org/10.1016/S0098-1354\(02\)00128-X](https://doi.org/10.1016/S0098-1354(02)00128-X), 2002.

85 Denby, B. R., Gauss, M., Wind, P., Mu, Q., Grøtting Wærsted, E., Fagerli, H., Valdebenito, A., and Klein, H.: Description of the
86 uEMEP_v5 downscaling approach for the EMEP MSC-W chemistry transport model, *Geoscientific Model Development*,
87 13, 6303–6323, <https://doi.org/10.5194/gmd-13-6303-2020>, 2020.

88 Dimitriou, K., Grivas, G., Liakakou, E., Gerasopoulos, E., and Mihalopoulos, N.: Assessing the contribution of regional
89 sources to urban air pollution by applying 3D-PSCF modeling, *Atmospheric Research*, 248, 105187,
90 <https://doi.org/10.1016/j.atmosres.2020.105187>, 2021.

91 Ding, J., Zhao, P., Su, J., Dong, Q., Du, X., and Zhang, Y.: Aerosol pH and its driving factors in Beijing, 19, 7939–7954,
92 <https://doi.org/10.5194/acp-19-7939-2019>, 2019.

93 Driscoll, C. T., Driscoll, K. M., Mitchell, M. J., and Raynal, D. J.: Effects of acidic deposition on forest and aquatic
94 ecosystems in New York State, *Environ Pollut*, 123, 327–336, [https://doi.org/10.1016/s0269-7491\(03\)00019-8](https://doi.org/10.1016/s0269-7491(03)00019-8), 2003.

95 Driscoll, C. T., Driscoll, K. M., Fakhraei, H., and Civerolo, K.: Long-term temporal trends and spatial patterns in the acid-
96 base chemistry of lakes in the Adirondack region of New York in response to decreases in acidic deposition, *Atmospheric*
97 *Environment*, 146, 5–14, <https://doi.org/10.1016/j.atmosenv.2016.08.034>, 2016.

98 Fameli, K.-M. and Assimakopoulos, V. D.: The new open Flexible Emission Inventory for Greece and the Greater Athens
99 Area (FEI-GREGAA): Account of pollutant sources and their importance from 2006 to 2012, *Atmospheric Environment*,
100 137, 17–37, <https://doi.org/10.1016/j.atmosenv.2016.04.004>, 2016.

101 Fountoukis, C. and Nenes, A.: ISORROPIA II: a computationally efficient thermodynamic equilibrium model for $K^+ - Ca^{2+} - Mg^{2+} - NH_4^+ - Na^+ - SO_4^{2-} - NO_3^-$, *Atmospheric Chemistry and Physics*, 7, 4639–4659, <https://doi.org/10.5194/acp-7-4639-2007>, 2007.

102 Fountoukis, C., Racherla, P. N., Denier van der Gon, H. a. C., Polymeneas, P., Charalampidis, P. E., Pilinis, C.,
103 Wiedensohler, A., Dall’Osto, M., O’Dowd, C., and Pandis, S. N.: Evaluation of a three-dimensional chemical transport
104 model (PMCAMx) in the European domain during the EUCAARI May 2008 campaign, *Atmospheric Chemistry and*
105 *Physics*, 11, 10331–10347, <https://doi.org/10.5194/acp-11-10331-2011>, 2011.

106 Fourtziou, L., Liakakou, E., Stavroulas, I., Theodosi, C., Zarnmpas, P., Psiloglou, B., Sciare, J., Maggos, T., Bairachtari, K.,
107 Bougiatioti, A., Gerasopoulos, E., Sarda-Estève, R., Bonnaire, N., and Mihalopoulos, N.: Multi-tracer approach to
108 characterize domestic wood burning in Athens (Greece) during wintertime, *Atmospheric Environment*, 148, 89–101,
109 <https://doi.org/10.1016/j.atmosenv.2016.10.011>, 2017.

110 Franklin, M., Koutrakis, P., and Schwartz, J.: The Role of Particle Composition on the Association Between PM_{2.5} and
111 Mortality, *Epidemiology*, 19, 680–689, <https://doi.org/10.1097/EDE.0b013e3181812bb7>, 2008.

112 Gong, S. L.: A parameterization of sea-salt aerosol source function for sub- and super-micron particles, *Global*
113 *Biogeochemical Cycles*, 17, <https://doi.org/10.1029/2003GB002079>, 2003.

114 Gratsea, M., Athanasopoulou, E., Kakouri, A., Richter, A., Seyler, A., and Gerasopoulos, E.: Five Years of Spatially
115 Resolved Ground-Based MAX-DOAS Measurements of Nitrogen Dioxide in the Urban Area of Athens: Synergies with In
116 Situ Measurements and Model Simulations, *Atmosphere*, 12, 1634, <https://doi.org/10.3390/atmos12121634>, 2021.

117 Grivas, G., Cheristanidis, S., Chaloulakou, A., Koutrakis, P., and Mihalopoulos, N.: Elemental Composition and Source
118 Apportionment of Fine and Coarse Particles at Traffic and Urban Background Locations in Athens, Greece, *Aerosol Air*
119 *Qual. Res.*, 18, 1642–1659, <https://doi.org/10.4209/aaqr.2017.12.0567>, 2018.

120 Grivas, G., Stavroulas, I., Liakakou, E., Kaskaoutis, D. G., Bougiatioti, A., Paraskevopoulou, D., Gerasopoulos, E., and
121 Mihalopoulos, N.: Measuring the spatial variability of black carbon in Athens during wintertime, *Air Qual Atmos Health*, 12,
122 1405–1417, <https://doi.org/10.1007/s11869-019-00756-y>, 2019.

26 Grivas, G., Athanasopoulou, E., Kakouri, A., Bailey, J., Liakakou, E., Stavroulas, I., Kalkavouras, P., Bougiatioti, A.,
 27 Kaskaoutis, D. G., Ramonet, M., Mihalopoulos, N., and Gerasopoulos, E.: Integrating in situ Measurements and City Scale
 28 Modelling to Assess the COVID-19 Lockdown Effects on Emissions and Air Quality in Athens, Greece, *Atmosphere*, 11,
 29 1174, <https://doi.org/10.3390/atmos11111174>, 2020.

30 Guevara, M., Jorba, O., Tena, C., Denier Van Der Gon, H., Kuenen, J., Elguindi, N., Darras, S., Granier, C., and Pérez
 31 García-Pando, C.: Copernicus Atmosphere Monitoring Service TEMPORal profiles (CAMS-TEMPO): global and European
 32 emission temporal profile maps for atmospheric chemistry modelling, *Earth Syst. Sci. Data*, 13, 367–404,
 33 <https://doi.org/10.5194/essd-13-367-2021>, 2021.

34 Guo, H., Xu, L., Bougiatioti, A., Cerully, K. M., Capps, S. L., Hite, J. R., Carlton, A. G., Lee, S.-H., Bergin, M. H., Ng, N.
 35 L., Nenes, A., and Weber, R. J.: Fine-particle water and pH in the southeastern United States, *Atmospheric Chemistry and
 36 Physics*, 15, 5211–5228, <https://doi.org/10.5194/acp-15-5211-2015>, 2015.

37 Guo, H., Sullivan, A. P., Campuzano-Jost, P., Schroder, J. C., Lopez-Hilfiker, F. D., Dibb, J. E., Jimenez, J. L., Thornton, J.
 38 A., Brown, S. S., Nenes, A., and Weber, R. J.: Fine particle pH and the partitioning of nitric acid during winter in the
 39 northeastern United States, *Journal of Geophysical Research: Atmospheres*, 121, 10,355–10,376,
 40 <https://doi.org/10.1002/2016JD025311>, 2016.

41 Guo, H., Liu, J., Froyd, K. D., Roberts, J. M., Veres, P. R., Hayes, P. L., Jimenez, J. L., Nenes, A., and Weber, R. J.: Fine
 42 particle pH and gas–particle phase partitioning of inorganic species in Pasadena, California, during the 2010 CalNex
 43 campaign, *Atmospheric Chemistry and Physics*, 17, 5703–5719, <https://doi.org/10.5194/acp-17-5703-2017>, 2017a.

44 Guo, H., Weber, R. J., and Nenes, A.: High levels of ammonia do not raise fine particle pH sufficiently to yield nitrogen
 45 oxide-dominated sulfate production, *Scientific Reports*, 7, 12109, <https://doi.org/10.1038/s41598-017-11704-0>, 2017b.

46 Guo, H., Nenes, A., and Weber, R. J.: The underappreciated role of nonvolatile cations in aerosol ammonium-sulfate molar
 47 ratios, *Atmos. Chem. Phys.*, 18, 17307–17323, <https://doi.org/10.5194/acp-18-17307-2018>, 2018.

48 Hamer, P. D., Walker, S.-E., Sousa-Santos, G., Vogt, M., Vo-Thanh, D., Lopez-Aparicio, S., Schneider, P., Ramacher, M. O.
 49 P., and Karl, M.: The urban dispersion model EPISODE v10.0 – Part 1: An Eulerian and sub-grid-scale air quality model and
 50 its application in Nordic winter conditions, *Geoscientific Model Development*, 13, 4323–4353, <https://doi.org/10.5194/gmd-13-4323-2020>, 2020.

51 Harris, E., Sinha, B., Pinxteren, D. V., Tilgner, A., Fomba, K. W., Schneider, J., Roth, A., Gnauk, T., Fahlbusch, B., Mertes,
 52 S., Lee, T., Collett, J., Foley, S., Borrmann, S., Hoppe, P., and Herrmann, H.: Enhanced Role of Transition Metal, *Science*,
 53 340, 727–730, <https://doi.org/10.1126/science.1230911>, 2013.

54 Hennigan, C. J., Izumi, J., Sullivan, A. P., Weber, R. J., and Nenes, A.: A critical evaluation of proxy methods used to
 55 estimate the acidity of atmospheric particles, *Atmospheric Chemistry and Physics*, 15, 2775–2790,
 56 <https://doi.org/10.5194/acp-15-2775-2015>, 2015.

57 Hurley, P. J., Physick, W. L., and Luhar, A. K.: TAPM: a practical approach to prognostic meteorological and air pollution
 58 modelling, *Environmental Modelling & Software*, 20, 737–752, <https://doi.org/10.1016/j.envsoft.2004.04.006>, 2005.

59 Im, U., Christodoulaki, S., Violaki, K., Zarmas, P., Kocak, M., Daskalakis, N., Mihalopoulos, N., and Kanakidou, M.:
 60 Atmospheric deposition of nitrogen and sulfur over southern Europe with focus on the Mediterranean and the Black Sea,
 61 *Atmospheric Environment*, 81, <https://doi.org/10.1016/j.atmosenv.2013.09.048>, 2013.

62 Karl, M. and Ramacher, M. O. P.: Urban Atmospheric Chemistry with the EPISODE-CityChem Model, in: *Air Pollution
 63 Modeling and its Application XXVII*, edited by: Mensink, C. and Matthias, V., Springer Berlin Heidelberg, Berlin,
 64 Heidelberg, 235–239, https://doi.org/10.1007/978-3-662-63760-9_33, 2021.

65 Karl, M., Walker, S.-E., Solberg, S., and Ramacher, M. O. P.: The Eulerian urban dispersion model EPISODE – Part 2:
 66 Extensions to the source dispersion and photochemistry for EPISODE–CityChem v1.2 and its application to the city of
 67 Hamburg, *Geoscientific Model Development*, 12, 3357–3399, <https://doi.org/10.5194/gmd-12-3357-2019>, 2019.

68 Karl, M., Ramacher, M. O. P., Oppo, S., Lanzi, L., Majamäki, E., Jalkanen, J.-P., Lanzafame, G. M., Temime-Roussel, B.,
 69 Le Berre, L., and D’Anna, B.: Measurement and Modeling of Ship-Related Ultrafine Particles and Secondary Organic
 70 Aerosols in a Mediterranean Port City, *Toxics*, 11, 771, <https://doi.org/10.3390/toxics11090771>, 2023.

71 Karydis, V. A., Tsimpidi, A. P., Pozzer, A., Astitha, M., and Lelieveld, J.: Effects of mineral dust on global atmospheric
 72 nitrate concentrations, *Atmospheric Chemistry and Physics*, 16, 1491–1509, <https://doi.org/10.5194/acp-16-1491-2016>,
 73 2016.

74 Koçak, M., Kubilay, N., and Mihalopoulos, N.: Ionic composition of lower tropospheric aerosols at a Northeastern

76 Mediterranean site: implications regarding sources and long-range transport, *Atmospheric Environment*, 38, 2067–2077,
77 <https://doi.org/10.1016/j.atmosenv.2004.01.030>, 2004.

78 Koçak, M., Theodosi, C., Zampas, P., Séguret, M. J. M., Herut, B., Kallos, G., Mihalopoulos, N., Kubilay, N., and Nimmo,
79 M.: Influence of mineral dust transport on the chemical composition and physical properties of the Eastern Mediterranean
80 aerosol, *Atmospheric Environment*, 57, 266–277, <https://doi.org/10.1016/j.atmosenv.2012.04.006>, 2012.

81 Kontos, S., Kakosimos, K., Liora, N., Poupkou, A., and Melas, D.: Towards a regional dust modeling system in the central
82 Middle East: Evaluation, uncertainties and recommendations, *Atmospheric Environment*, 246, 118160,
83 <https://doi.org/10.1016/j.atmosenv.2020.118160>, 2021.

84 Koulouri, E., Saarikoski, S., Theodosi, C., Markaki, Z., Gerasopoulos, E., Kouvarakis, G., Mäkelä, T., Hillamo, R., and
85 Mihalopoulos, N.: Chemical composition and sources of fine and coarse aerosol particles in the Eastern Mediterranean,
86 *Atmospheric Environment*, 42, 6542–6550, <https://doi.org/10.1016/j.atmosenv.2008.04.010>, 2008.

87 Kushta, J., Georgiou, G. K., Proestos, Y., Christoudias, T., Thunis, P., Savvides, C., Papadopoulos, C., and Lelieveld, J.:
88 Evaluation of EU air quality standards through modeling and the FAIRMODE benchmarking methodology, *Air Qual Atmos*
89 *Health*, 12, 73–86, <https://doi.org/10.1007/s11869-018-0631-z>, 2019.

90 Lasne, J., Lostier, A., Salameh, T., Athanasopoulou, E., Karagiannis, D., Kakouri, A., Vassaux, S., Lesueur, D., and
91 Romanias, M. N.: NO_x emissions by real-world fresh and old asphalt mixtures: Impact of temperature, relative humidity,
92 and UV-irradiation, *Urban Climate*, 49, 101457, <https://doi.org/10.1016/j.uclim.2023.101457>, 2023.

93 Lawal, A. S., Guan, X., Liu, C., Henneman, L. R. F., Vasilakos, P., Bhogineni, V., Weber, R. J., Nenes, A., and Russell, A.
94 G.: Linked Response of Aerosol Acidity and Ammonia to SO₂ and NO_x Emissions Reductions in the United States,
95 *Environmental Science & Technology*, 52, 9861–9873, <https://doi.org/10.1021/acs.est.8b00711>, 2018.

96 Lee-Taylor, J. and Madronich, S.: Calculation of actinic fluxes with a coupled atmosphere–snow radiative transfer model, *J.-*
97 *Geophys.-Res.*, 107, <https://doi.org/10.1029/2002JD002084>, 2002.

98 Liakakou, E., Fountziou, L., Paraskevopoulou, D., Speyer, O., Lianou, M., Grivas, G., Myriokefalitakis, S., and
99 Mihalopoulos, N.: High-Resolution Measurements of SO₂, HNO₃ and HCl at the Urban Environment of Athens, Greece:
00 Levels, Variability and Gas to Particle Partitioning, *Atmosphere*, 13, 218, <https://doi.org/10.3390/atmos13020218>, 2022.

01 Liakakou, E., Mihalopoulos, N., Theodosi, C., Tsiotra, E., Kaskaoutis, D. G., Koukouli, M.-E., Balis, D., Kharol, S. K.,
02 Shephard, M. W., Dammers, E., and Cady-Pereira, K. E.: Inorganic Aerosol Precursors in the Mediterranean Atmosphere,
03 in: *Atmospheric Chemistry in the Mediterranean Region: Volume 1 - Background Information and Pollutant Distribution*,
04 edited by: Dulac, F., Sauvage, S., and Hamonou, E., Springer International Publishing, Cham, 471–503,
05 https://doi.org/10.1007/978-3-031-12741-0_14, 2023.

06 Liao, H., Adams, P. J., Chung, S. H., Seinfeld, J. H., Mickley, L. J., and Jacob, D. J.: Interactions between tropospheric
07 chemistry and aerosols in a unified general circulation model, *Journal of Geophysical Research*, 108, 4001,
08 <https://doi.org/10.1029/2001JD001260>, 2003.

09 Liora, N., Kontos, S., Parliari, D., Akritidis, D., Poupkou, A., Papanastasiou, D. K., and Melas, D.: “On-Line” Heating
10 Emissions Based on WRF Meteorology—Application and Evaluation of a Modeling System over Greece, *Atmosphere*, 13,
11 568, <https://doi.org/10.3390/atmos13040568>, 2022.

12 Liu, M., Huang, X., Song, Y., Tang, J., Cao, J., Zhang, X., Zhang, Q., Wang, S., Xu, T., Kang, L., Cai, X., Zhang, H., Yang,
13 F., Wang, H., Yu, J. Z., Lau, A. K. H., He, L., Huang, X., Duan, L., Ding, A., Xue, L., Gao, J., Liu, B., and Zhu, T.:
14 Ammonia emission control in China would mitigate haze pollution and nitrogen deposition, but worsen acid rain,
15 *Proceedings of the National Academy of Sciences*, 116, 7760–7765, <https://doi.org/10.1073/pnas.1814880116>, 2019.

16 Liu, T., Chan, A. W. H., and Abbatt, J. P. D.: Multiphase Oxidation of Sulfur Dioxide in Aerosol Particles: Implications for
17 Sulfate Formation in Polluted Environments, <https://doi.org/10.1021/acs.est.0c06496>, 2021.

18 Mantas, E., Remoundaki, E., Halari, I., Kassomenos, P., Theodosi, C., Hatzikioseyan, A., and Mihalopoulos, N.: Mass
19 closure and source apportionment of PM_{2.5} by Positive Matrix Factorization analysis in urban Mediterranean environment,
20 *Atmospheric Environment*, 94, 154–163, <https://doi.org/10.1016/j.atmosenv.2014.05.002>, 2014.

21 Myhre, G., Shindell, D., Pongratz, J., and Stocker, T.: *Anthropogenic and Natural Radiative Forcing*, edited by: Stocker, T.,
22 Ludwig-Maximilians-Universität München, Cambridge, 659–740, <https://doi.org/10.1017/CBO9781107415324.018>, 2014.

23 Myriokefalitakis, S., Daskalakis, N., Gkouvousis, A., Hilboll, A., van Noije, T., Williams, J. E., Le Sager, P., Huijnen, V.,
24 Houweling, S., Bergman, T., Nüß, J. R., Vrekoussis, M., Kanakidou, M., and Krol, M. C.: Description and evaluation of a
25 detailed gas-phase chemistry scheme in the TM5-MP global chemistry transport model (r112), *Geoscientific Model*

26 Development, 13, 5507–5548, <https://doi.org/10.5194/gmd-13-5507-2020>, 2020.

27 Myriokefalitakis, S., Bergas-Massó, E., Gonçalves-Ageitos, M., Pérez García-Pando, C., van Noije, T., Le Sager, P., Ito, A.,
28 Athanasopoulou, E., Nenes, A., Kanakidou, M., Krol, M. C., and Gerasopoulos, E.: Multiphase processes in the EC-Earth
29 model and their relevance to the atmospheric oxalate, sulfate, and iron cycles, *Geoscientific Model Development*, 15, 3079–
30 3120, <https://doi.org/10.5194/gmd-15-3079-2022>, 2022.

31 Nenes, A., Pandis, S. N., and Pilinis, C.: ISORROPIA: A New Thermodynamic Equilibrium Model for Multiphase
32 Multicomponent Inorganic Aerosols, *Aquatic Geochemistry*, 4, 123–152, <https://doi.org/10.1023/A:1009604003981>, 1998.

33 Nenes, A., Pandis, S. N., Weber, R. J., and Russell, A.: Aerosol pH and liquid water content determine when particulate
34 matter is sensitive to ammonia and nitrate availability, *Atmospheric Chemistry and Physics*, 20, 3249–3258,
35 <https://doi.org/10.5194/acp-20-3249-2020>, 2020.

36 Ng, N. L., Herndon, S. C., Trimborn, A., Canagaratna, M. R., Croteau, P. L., Onasch, T. B., Sueper, D., Worsnop, D. R.,
37 Zhang, Q., Sun, Y. L., and Jayne, J. T.: An Aerosol Chemical Speciation Monitor (ACSM) for Routine Monitoring of the
38 Composition and Mass Concentrations of Ambient Aerosol, *Aerosol Science and Technology*, 45, 780–794,
39 <https://doi.org/10.1080/02786826.2011.560211>, 2011.

40 Ozga, I., Bonazza, A., Ait Lyazidi, S., Haddad, M., Ben-Ncer, A., Ghedini, N., and Sabbioni, C.: Pollution impact on the
41 ancient ramparts of the Moroccan city Salé, *Journal of Cultural Heritage*, 14, S25–S33,
42 <https://doi.org/10.1016/j.culher.2012.10.018>, 2013.

43 Panopoulou, A., Liakakou, E., Sauvage, S., Gros, V., Locoge, N., Stavroulas, I., Bonsang, B., Gerasopoulos, E., and
44 Mihalopoulos, N.: Yearlong measurements of monoterpenes and isoprene in a Mediterranean city (Athens): Natural vs
45 anthropogenic origin, *Atmospheric Environment*, 243, 117803, <https://doi.org/10.1016/j.atmosenv.2020.117803>, 2020.

46 Paraskevopoulou, D., Liakakou, E., Gerasopoulos, E., Theodosi, C., and Mihalopoulos, N.: Long-term characterization of
47 organic and elemental carbon in the PM_{2.5} fraction: the case of Athens, Greece, *Atmos. Chem. Phys.*, 14, 13313–13325,
48 <https://doi.org/10.5194/acp-14-13313-2014>, 2014.

49 Paraskevopoulou, D., Liakakou, E., Gerasopoulos, E., and Mihalopoulos, N.: Sources of atmospheric aerosol from long-term
50 measurements (5years) of chemical composition in Athens, Greece, *Science of The Total Environment*, 527–528, 165–178,
51 <https://doi.org/10.1016/j.scitotenv.2015.04.022>, 2015.

52 Pope, C. A., Coleman, N., Pond, Z. A., and Burnett, R. T.: Fine particulate air pollution and human mortality: 25+ years of
53 cohort studies, *Environmental Research*, 183, 108924, <https://doi.org/10.1016/j.envres.2019.108924>, 2020.

54 Pringle, K. J., Tost, H., Metzger, S., Steil, B., Giannadaki, D., Nenes, A., Fountoukis, C., Stier, P., Vignati, E., and Lelieveld,
55 J.: Description and evaluation of GMXe: a new aerosol submodel for global simulations (v1), *Geoscientific Model
56 Development*, 3, 413–413, <https://doi.org/10.5194/gmd-3-413-2010>, 2010.

57 Pye, H. O. T., Nenes, A., Alexander, B., Ault, A. P., Barth, M. C., Clegg, S. L., Collett, J. L., Fahey, K. M., Hennigan, C. J.,
58 Herrmann, H., Kanakidou, M., Kelly, J. T., Ku, I. T., Faye McNeill, V., Riemer, N., Schaefer, T., Shi, G., Tilgner, A.,
59 Walker, J. T., Wang, T., Weber, R., Xing, J., Zaveri, R. A., and Zuend, A.: The acidity of atmospheric particles and clouds,
60 *Atmospheric Chemistry and Physics*, 20, 4809–4888, <https://doi.org/10.5194/acp-20-4809-2020>, 2020.

61 Ramacher, M. O. P., Kakouri, A., Speyer, O., Feldner, J., Karl, M., Timmermans, R., Denier van der Gon, H., Kuenen, J.,
62 Gerasopoulos, E., and Athanasopoulou, E.: The UrbEm Hybrid Method to Derive High-Resolution Emissions for City-Scale
63 Air Quality Modeling, *Atmosphere*, 12, 1404, <https://doi.org/10.3390/atmos12111404>, 2021.

64 Salter, M. E., Zieger, P., Acosta Navarro, J. C., Grythe, H., Kirkevåg, A., Rosati, B., Riipinen, I., and Nilsson, E. D.: An
65 empirically derived inorganic sea spray source function incorporating sea surface temperature, *Atmospheric Chemistry and
66 Physics*, 15, 11047–11066, <https://doi.org/10.5194/acp-15-11047-2015>, 2015.

67 Sander, R.: Compilation of Henry’s law constants (version 4.0) for water as solvent, *Atmospheric Chemistry and Physics*,
68 15, 4399–4981, <https://doi.org/10.5194/acp-15-4399-2015>, 2015.

69 Sandu, A. and Sander, R.: Technical note: Simulating chemical systems in Fortran90 and Matlab with the Kinetic
70 PreProcessor KPP-2.1, *Atmospheric Chemistry and Physics*, 6, 187–195, <https://doi.org/10.5194/acp-6-187-2006>, 2006.

71 Santiago, J. L., Rivas, E., Gamarra, A. R., Vivanco, M. G., Buccolieri, R., Martilli, A., Lechón, Y., and Martín, F.: Estimates
72 of population exposure to atmospheric pollution and health-related externalities in a real city: The impact of spatial
73 resolution on the accuracy of results, *Science of The Total Environment*, 819, 152062,
74 <https://doi.org/10.1016/j.scitotenv.2021.152062>, 2022.

75 Sarnat, S. E., Winquist, A., Schauer, J. J., Turner, J. R., and Sarnat, J. A.: Fine Particulate Matter Components and

76 Emergency Department Visits for Cardiovascular and Respiratory Diseases in the St. Louis, Missouri–Illinois, Metropolitan
77 Area, *Environ Health Perspect*, 123, 437–444, <https://doi.org/10.1289/ehp.1307776>, 2015.

78 Sciare, J., Oikonomou, K., Cachier, H., Mihalopoulos, N., Andreae, M. O., Maenhaut, W., and Sarda-Estève, R.: Aerosol
79 mass closure and reconstruction of the light scattering coefficient over the Eastern Mediterranean Sea during the MINOS
80 campaign, *Atmospheric Chemistry and Physics*, 5, 2253–2265, <https://doi.org/10.5194/acp-5-2253-2005>, 2005.

81 Seinfeld, J. H. and Pandis, S. N.: *Atmospheric Chemistry and Physics: From Air Pollution to Climate Change*, 2006.

82 Slørdal, L. H., McInnes, H., and Krognes, T.: The Air Quality Management System AirQUIS, in: *Information Technologies
83 in Environmental Engineering*, Berlin, Heidelberg, 21–33, https://doi.org/10.1007/978-3-540-71335-7_6, 2007.

84 Sokhi, R. S., Moussiopoulos, N., Baklanov, A., Bartzis, J., Coll, I., Finardi, S., Friedrich, R., Geels, C., Grönholm, T.,
85 Halenka, T., Ketzel, M., Maragkidou, A., Matthias, V., Moldanova, J., Ntziachristos, L., Schäfer, K., Suppan, P., Tsegas, G.,
86 Carmichael, G., Franco, V., Hanna, S., Jalkanen, J.-P., Velders, G. J. M., and Kukkonen, J.: Advances in air quality research
87 – current and emerging challenges, *Atmos. Chem. Phys.*, 22, 4615–4703, <https://doi.org/10.5194/acp-22-4615-2022>, 2022.

88 Sposito, G.: *The Chemistry of Soils*, Oxford University Press, Oxford, 277 pp., 1989.

89 Stavroulas, I., Bougiatioti, A., Grivas, G., Paraskevopoulou, D., Tsagkaraki, M., Zarmpas, P., Liakakou, E., Gerasopoulos,
90 E., and Mihalopoulos, N.: Sources and processes that control the submicron organic aerosol composition in an urban
91 Mediterranean environment (Athens): a high temporal-resolution chemical composition measurement study, *Atmospheric
92 Chemistry and Physics*, 19, 901–919, <https://doi.org/10.5194/acp-19-901-2019>, 2019.

93 Stavroulas, I., Grivas, G., Liakakou, E., Kalkavouras, P., Bougiatioti, A., Kaskaoutis, D. G., Lianou, M., Papoutsidaki, K.,
94 Tsagkaraki, M., Zarmpas, P., Gerasopoulos, E., and Mihalopoulos, N.: Online Chemical Characterization and Sources of
95 Submicron Aerosol in the Major Mediterranean Port City of Piraeus, Greece, *Atmosphere*, 12, 1686,
96 <https://doi.org/10.3390/atmos12121686>, 2021.

97 Theodosi, C., Tsagkaraki, M., Zarmpas, P., Grivas, G., Liakakou, E., Paraskevopoulou, D., Lianou, M., Gerasopoulos, E.,
98 and Mihalopoulos, N.: Multi-year chemical composition of the fine-aerosol fraction in Athens, Greece, with emphasis on the
99 contribution of residential heating in wintertime, *Atmospheric Chemistry and Physics*, 18, 14371–14391,
00 <https://doi.org/10.5194/acp-18-14371-2018>, 2018.

01 Vignati, E., Facchini, M. C., Rinaldi, M., Scannell, C., Ceburnis, D., Sciare, J., Kanakidou, M., Myriokefalitakis, S.,
02 Dentener, F., and O'Dowd, C. D.: Global scale emission and distribution of sea-spray aerosol: Sea-salt and organic
03 enrichment, *Atmospheric Environment*, 44, 670–677, <https://doi.org/10.1016/j.atmosenv.2009.11.013>, 2010.

04 Wang, T., Liu, Y., Cheng, H., Wang, Z., Fu, H., Chen, J., and Zhang, L.: Significant formation of sulfate aerosols
05 contributed by the heterogeneous drivers of dust surface, *Atmospheric Chemistry and Physics*, 22, 13467–13493,
06 <https://doi.org/10.5194/acp-22-13467-2022>, 2022.

07 Watmough, S. A., Eimers, C., and Baker, S.: Impediments to recovery from acid deposition, *Atmospheric Environment*, 146,
08 15–27, <https://doi.org/10.1016/j.atmosenv.2016.03.021>, 2016.

09 WHO: WHO global air quality guidelines: particulate matter (PM_{2.5} and PM₁₀), ozone, nitrogen dioxide, sulfur dioxide and
10 carbon monoxide, , xxi, 273 p., 2021.

11 Williams, J. E., van Velthoven, P. F. J., and Brenninkmeijer, C. A. M.: Quantifying the uncertainty in simulating global
12 tropospheric composition due to the variability in global emission estimates of Biogenic Volatile Organic Compounds,
13 *Atmospheric Chemistry and Physics*, 13, 2857–2891, <https://doi.org/10.5194/acp-13-2857-2013>, 2013.

14 Williams, J. E., Boersma, K. F., Le Sager, P., and Verstraeten, W. W.: The high-resolution version of TM5-MP for
15 optimized satellite retrievals: description and validation, *Geoscientific Model Development*, 10, 721–750,
16 <https://doi.org/10.5194/gmd-10-721-2017>, 2017.

17 Yarwood, G., Rao, S., and Yocke, M.: Updates to the carbon bond chemical mechanism: CB05 - Prepared for Deborah
18 Luecken U.S. Environmental Protection Agency Research Triangle Park, NC 27703, YOCKE AND COMPANY, 2005.

19 Zakoura, M. and Pandis, S. N.: Overprediction of aerosol nitrate by chemical transport models: The role of grid resolution,
20 *Atmospheric Environment*, 187, 390–400, <https://doi.org/10.1016/j.atmosenv.2018.05.066>, 2018.

21 Zhang, L., Wang, T., Zhang, Q., Zheng, J., Xu, Z., and Lv, M.: Potential sources of nitrous acid (HONO) and their impacts
22 on ozone: A WRF-Chem study in a polluted subtropical region: MODELING HONO IN A SUBTROPICAL REGION, *J.
23 Geophys. Res. Atmos.*, 121, 3645–3662, <https://doi.org/10.1002/2015JD024468>, 2016.

24 Zhang, Y., Yang, Y., Zhang, L., Xu, H., Sun, J., Wang, T., Li, F., Chang, X., Ho, S. S. H., Li, B., Wang, B., Cao, J., and
25 Shen, Z.: Insight into the contributions of primary emissions of sulfate, nitrate, and ammonium from residential solid fuels to

26 ambient PM_{2.5}, *Atmospheric Research*, 290, 106790, <https://doi.org/10.1016/j.atmosres.2023.106790>, 2023.
27 Zhang, Z., Gao, J., Engling, G., Tao, J., Chai, F., Zhang, L., Zhang, R., Sang, X., Chan, C., Lin, Z., and Cao, J.:
28 Characteristics and applications of size-segregated biomass burning tracers in China's Pearl River Delta region, *Atmospheric*
29 *Environment*, 102, 290–301, <https://doi.org/10.1016/j.atmosenv.2014.12.009>, 2015.
30 Zhang, Z.-H., Hartner, E., Uttinger, B., Gfeller, B., Paul, A., Sklorz, M., Czech, H., Yang, B. X., Su, X. Y., Jakobi, G.,
31 Orasche, J., Schnelle-Kreis, J., Jeong, S., Gröger, T., Pardo, M., Hohaus, T., Adam, T., Kiendler-Scharr, A., Rudich, Y.,
32 Zimmermann, R., and Kalberer, M.: Are reactive oxygen species (ROS) a suitable metric to predict toxicity of carbonaceous
33 aerosol particles?, *Atmospheric Chemistry and Physics*, 22, 1793–1809, <https://doi.org/10.5194/acp-22-1793-2022>, 2022.
34

35 Author contributions. SM made the couplings for including thermodynamic calculations in the model, developed the chemistry
36 code, performed the simulations, and evaluated the model. MK was responsible for all developments, updates, and maintenance
37 of the CityChem extension of the model. EA and AK developed the emission fields. KAW contributed to the creation of the
38 emission and boundary fields. DK and GP performed the meteorological simulations, developed and provided model
39 evaluation tools, and collected observational meteorological data. GG prepared and provided data for the preparation of
40 potassium emission fields from anthropogenic wood-burning processes. AB, EL, IS, GG, DP, and NM collected, prepared,
41 and provided atmospheric data used for model evaluation. SM, MK, EA, OS, and EG developed the methodology for this
42 work. SM conceptualized and wrote the paper, and all co-authors contributed to the preparation, the discussion of the results,
43 and provided comments on the final version of the paper.

44

45 Competing interests. The authors declare that they have no conflict of interest.

46

47 **Acknowledgments.** This work was supported by the EU H2020 project Research Infrastructures Services Reinforcing Air
48 Quality Monitoring Capacities in European Urban & Industrial AreaS (RI-URBANS) (grant 101036245). This work was
49 supported by computational time granted from the National Infrastructures for Research and Technology S.A. (GRNET S.A.)
50 in the National HPC facility – ARIS – under project ID 014008 (ANIONIC). The authors would like to thank A. Nenes for the
51 disposal of the ISORROPIA II code used for this work. The authors thank V. Kotroni and C. Lagouvardos for the use of in
52 situ measurements from the weather station network operated by the METEO unit of the National Observatory of Athens. The
53 authors are also grateful to two anonymous reviewers for their comments, which contributed significantly to the improvement
54 of the final version of this paper.

55

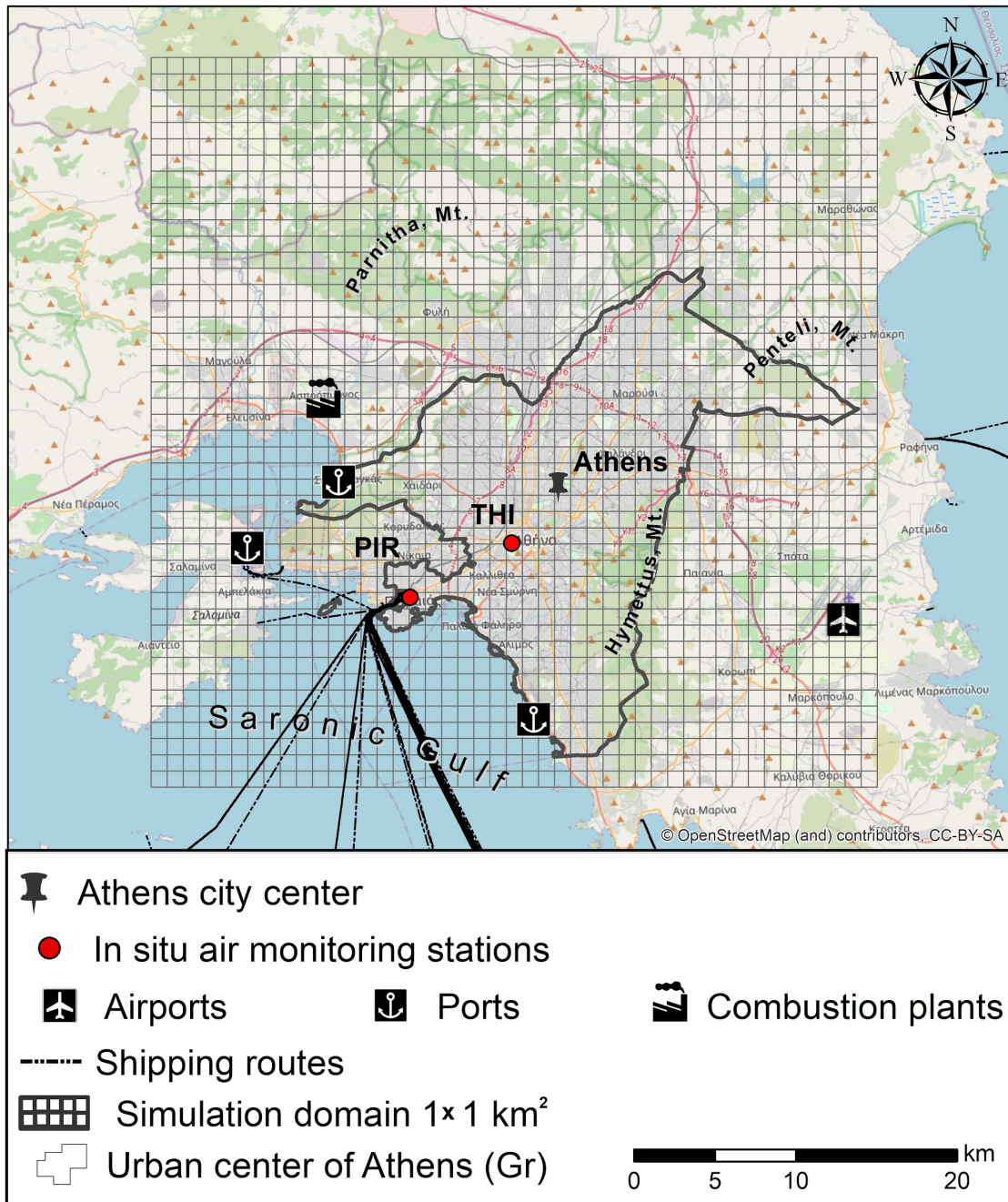
56 **Code and data availability.** The source codes of the EPISODE-CityChem model version 1.8 and the preprocessing utilities
57 are accessible in the release under the RPL license at <https://doi.org/10.5281/zenodo.8063985>. The thermodynamic equilibrium
58 model ISORROPIA II is available at <https://www.epfl.ch/labs/lapi/software/isorrophia/>.

59

61 Table 1. Reaction rates and constants used in EPISODE-CityChem for this study.

Reaction	Rate	Reference
	<i>Gas-phase chemistry rates (cm³ mol⁻¹ s⁻¹)</i>	
SO ₂ (g) + OH(g) → H ₂ SO ₄ (g) + HO ₂ (g)	k ₀ = 2.8 × 10 ⁻³¹ (T/300) ^{-2.6} × [N ₂] k _∞ = 2.0 × 10 ⁻¹² F _c = 0.75	1
	<i>Aqueous-phase chemistry rates (l mol⁻¹ s⁻¹)</i>	
HSO ₃ ⁻ + H ₂ O ₂ (+ H ⁺) → H ₂ SO ₄ (aq) + O ₂ (aq)	7.5 × 10 ⁷ e ^{-4430(1/T - 1/298)} × [H ⁺]/(1 + 13.0 × [H ⁺])	2
SO ₂ (aq) + O ₃ (aq) (+ H ₂ O) → S(VI)	2.4 × 10 ⁴	
HSO ₃ ⁻ + O ₃ → HSO ₄ ⁻ + O ₂ (aq)	3.7 × 10 ⁵ e ^{-5530(1/T - 1/298)}	2
SO ₃ ²⁻ + O ₃ → SO ₄ ²⁻ + O ₂ (aq)	1.5 × 10 ⁹ e ^{-5280(1/T - 1/298)}	2
	<i>Dissociation constants (mol l⁻¹)</i>	
SO ₂ (aq) ↔ SO ₃ ⁻ + H ⁺	1.3 × 10 ⁻² e ^{1960(1/T - 1/298)}	2
SO ₃ ⁻ ↔ SO ₃ ²⁻ + H ⁺	6.6 × 10 ⁻⁸ e ^{1500(1/T - 1/298)}	2
NH ₃ (aq) ↔ NH ₄ ⁺ + HO ⁻	1.7 × 10 ⁻⁵ e ^{-450(1/T - 1/298)}	2
CO ₂ (aq) ↔ HCO ₃ ⁻ + H ⁺	4.3 × 10 ⁻⁷ e ^{-1000(1/T - 1/298)}	2
HCO ₃ ⁻ ↔ CO ₃ ²⁻ + H ⁺	4.68 × 10 ⁻¹¹ e ^{-1760(1/T - 1/298)}	2
	<i>Henry law constants (mol m⁻³ Pa⁻¹)</i>	
SO ₂	1.3 × 10 ⁻² e ^{2900(1/T - 1/298)}	3
H ₂ O ₂	9.1 × 10 ² e ^{6600(1/T - 1/298)}	3
O ₃	1.0 × 10 ⁻⁴ e ^{2800(1/T - 1/298)}	3
CO ₂	3.3 × 10 ⁻⁴ e ^{2400(1/T - 1/298)}	3
NH ₃	5.9 × 10 ⁻¹ e ^{4200(1/T - 1/298)}	3
	<i>Heterogeneous chemistry</i>	
SO ₂ (g) {+ Dust} → H ₂ SO ₄	γ = 1.0 × 10 ⁻¹ (RH > 50%) γ = 3.0 × 10 ⁻¹ (RH < 50%)	4

¹ (Atkinson et al., 2004); ² (Seinfeld and Pandis, 2006); ³ (Sander, 2015); ⁴ (Liao et al., 2003)

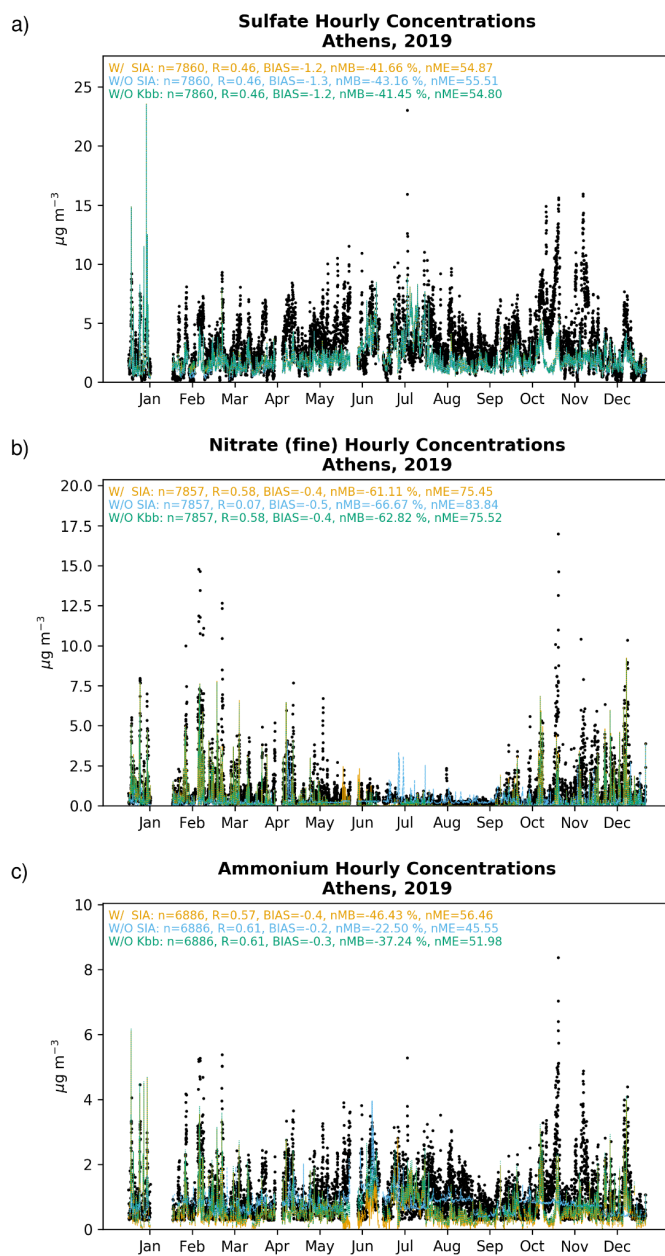


64

65

66

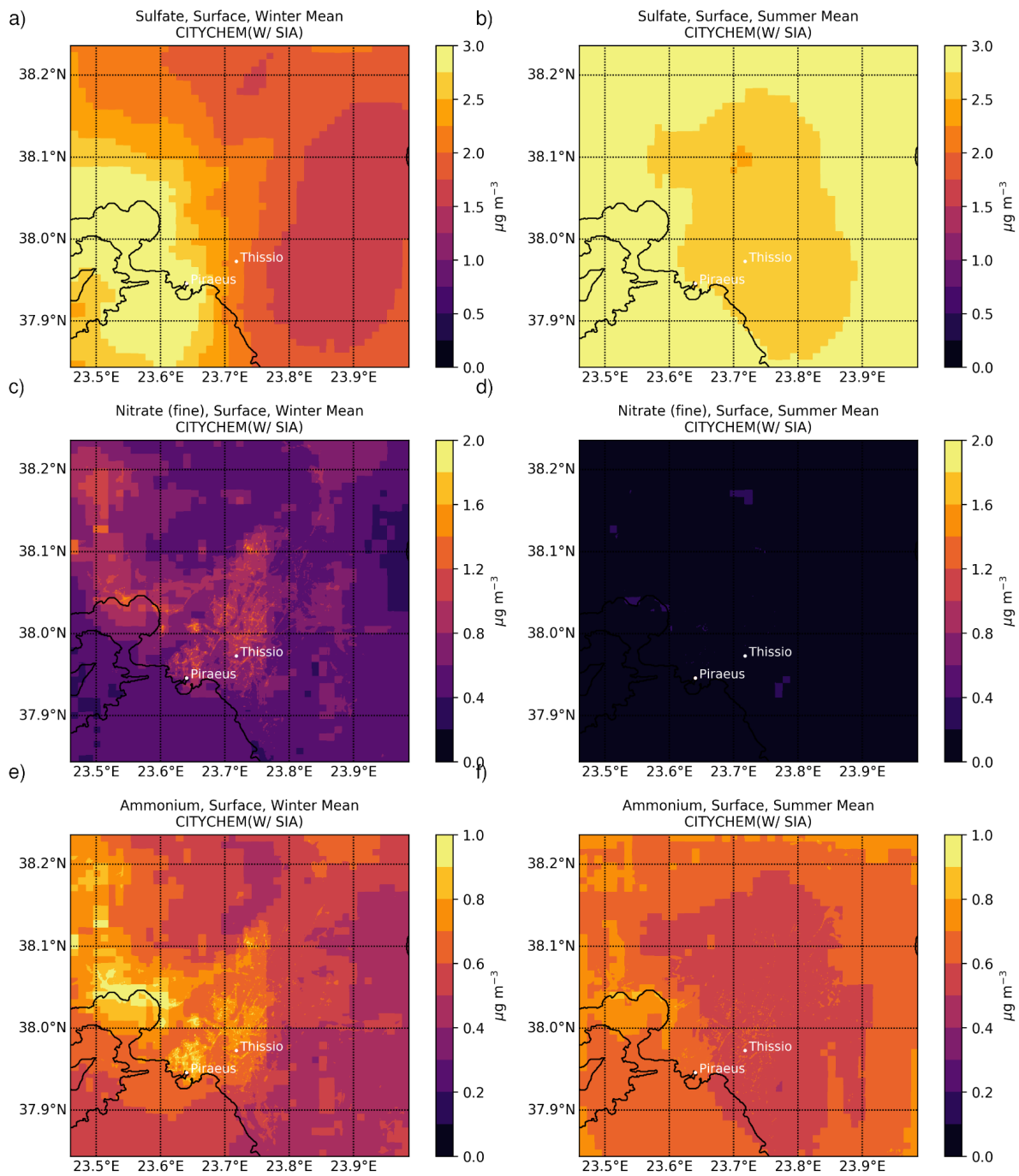
Figure 1. Model domain of the Greater Area of Athens, Greece. The gridded rectangles correspond to the air quality simulation domains. Sites (red dots) correspond to the air quality measurement stations during the simulation periods.



68

69 **Figure 2: Comparison ($\mu\text{g m}^{-3}$) of hourly mean observations (black dots) in Piraeus (1-16 January 2019; 11 June - 9 July 2019) and**
70 **in Thessio (17 January - 10 June 2019; 10 July - 31 December 2019) for a) sulfate, b) fine nitrate, and c) ammonium, to the EPISODE-**
71 **CityChem simulations for base case simulation (W/ SIA; orange line), without considering SIA formation (W/O SIA; blue line) and**
72 **without considering the contribution of K^+ from domestic heating processes in thermodynamic calculations (W/O Kbb; green line).**
73 **The respective correlation statistics are also provided.**

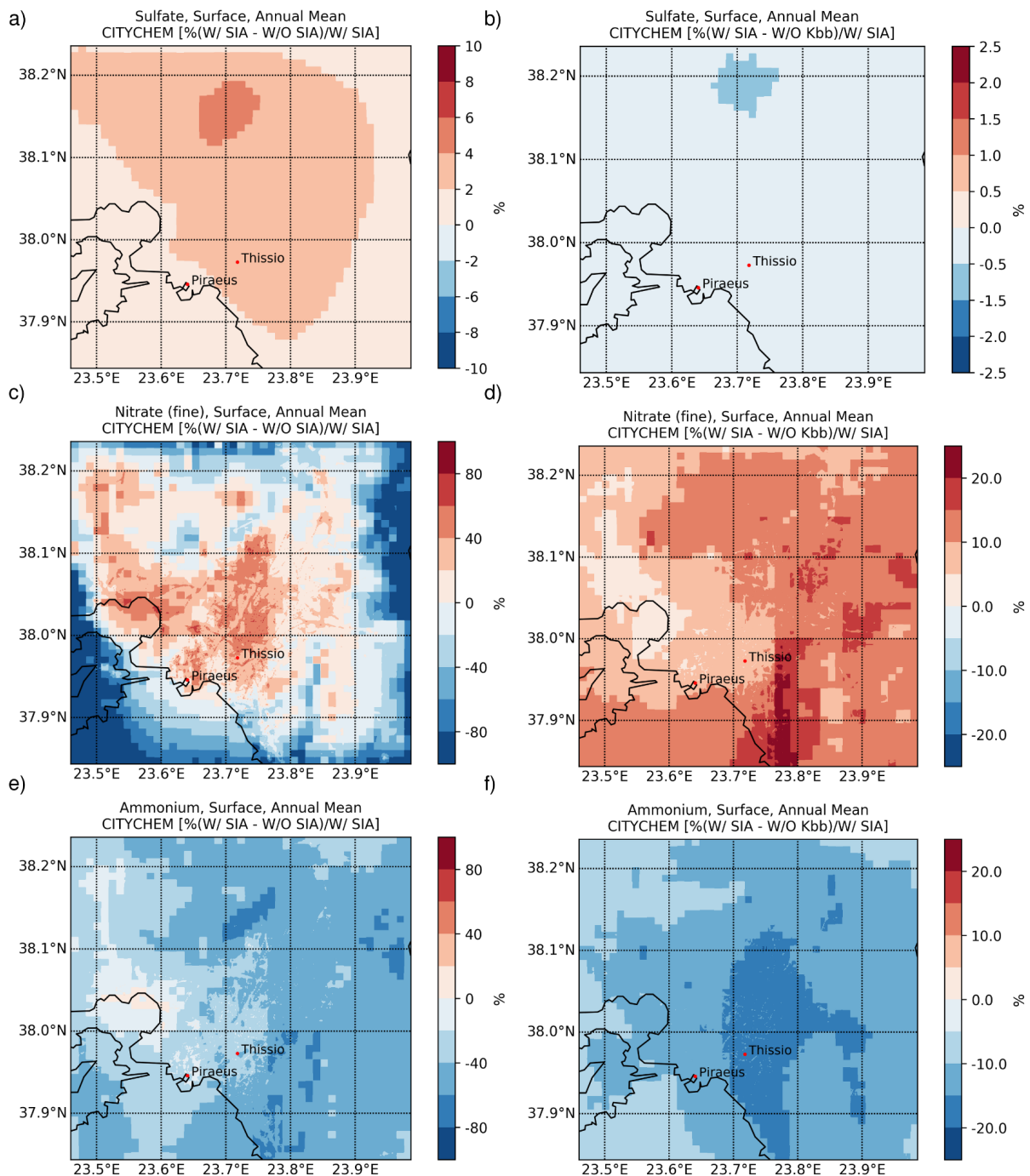
74



75

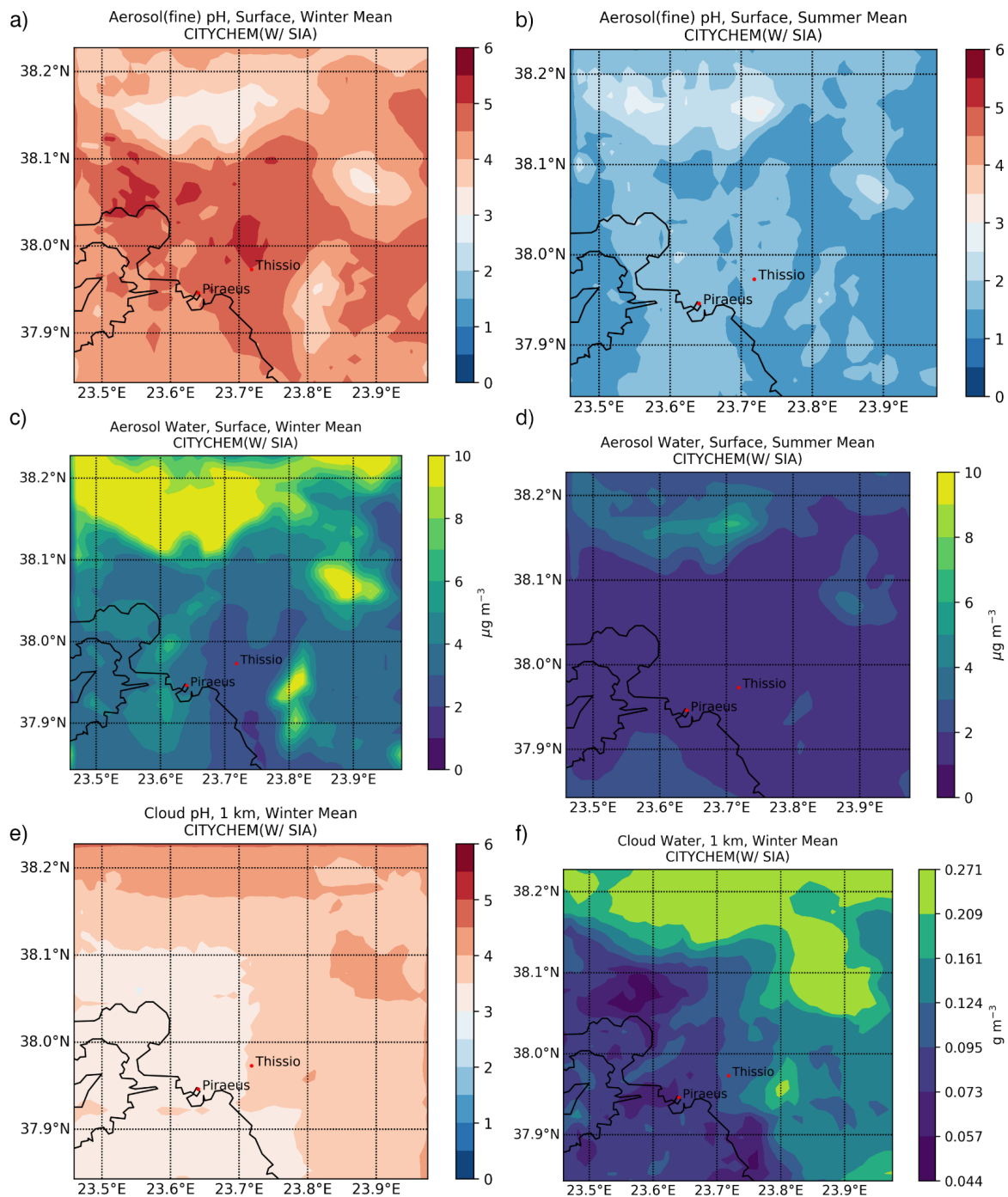
76 **Figure 3: Surface concentrations ($\mu\text{g m}^{-3}$) over the Greater Area of Athens of sulfate (a,b), nitrate (c,d), and ammonium (e,f), as**
 77 **simulated by EPISODE-CityChem on a horizontal resolution of $100 \times 100 \text{ m}^2$ for winter (December, January, and February; a,c,e)**
 78 **and summer (June, July, and August; b,d,f) of the year 2019.**

79



80
81
82
83
84

Figure 4: Annual mean percentage (%) contribution of secondary formation processes to the surface concentrations of sulfate (a), nitrate (c), and ammonium (e), and the respective impact of including the K^+ from domestic burning in thermodynamic calculations (b,d,f), as simulated by EPISODE-CityChem on a horizontal resolution of $100 \times 100 \text{ m}^2$ over the Greater Area of Athens for the year 2019.



85

86 **Figure 5:** Surface fine aerosol pH (a,b) and aerosol water content (c,d; $\mu\text{g m}^{-3}$) for winter (December, January, February; a,c) and
 87 summer (June, July, August; b,d) 2019, along with the cloud pH at 1 km altitude for winter (e) as simulated by EPISODE-CityChem
 88 on a horizontal resolution of $1 \times 1 \text{ km}^2$ over the Greater Area of Athens. The respective cloud water content (g m^{-3}) is also presented
 89 (g).